NANOSCALE APPROACHESFOR

BIOMOLECULE SEPARTION

AND DETECTION


by


SWATI GOYAL


Presented to the Faculty of the Graduate School of

The University of Texas at Arlington in Partial Fulfillment

of the Requirements

for the Degree of


MASTER IN SCIENCE IN BIOMEDICAL ENGINEERING


THE UNIVERSITY OF TEXAS AT ARLINGTON

DECEMBER 2009

ACKNOWLEDGEMENTS

ABSTRACT

NANOSCALE APPROACHESFOR

BIOMOLECULE SEPARTION

AND DETECTION

Swati Goyal, M.S.

The University of Texas at Arlington, 2009

Supervising Professor:  Samir Iqbal

Nanotechnology has the potential to contact and impact the biological interactions at the most basic chemical and physical levels.  New approaches to nanodevices allow high sensitivity and specificity with low sample requirement. Such devices are potential candidates for early disease detection at molecular levels and have important implications in associated therapeutics.

This research work focuses on two different areas: developing devices for DNA detection, protein enrichment and exploring material properties to fabricate microscale/nanoscale structures. In one approach, hairpin probe DNA was used to detect fmol of ss-DNA from *k-ras* oncogene.  In another approach, nanochannel based device was developed to selectively increase the concentration of one protein from a mixture of proteins taking advantage of antigen-antibody interactions in nanochannels. The phenomenon was demonstrated with selective separation of BSA and human hemoglobin.  Further, effect of fluorescence on fluid flow through channels was studied.

Towards biocompatible membranes, a rapid, simple and inexpensive approach to fabricate microchannels from 100-700 micron was developed. These channels were made in PDMS using simple chemistry and materials like nanoparticles, polyurethane and acetone, at various curing temperatures.

TABLE OF CONTENTS

LIST OF ILLUSTRATIONS

ix

LIST OF TABLES

CHAPTER 1

INTRODUCTION

Nanobiotechnology is the product of merger between biology and various engineering fields that facilitate the tools to elucidate, manipulate and quantify the biomolecule at the most fundamental level. These tools are capable to read single molecule in physical dimensions which was not possible before in macro world. The biology inspires the scientists for bottom up approach to fabricate synthetic self assembled layers and in return the tools operating at nanoscale unravel the physics and chemical behavior of biomolecules in unprecedented details. Interestingly, the biomolecules and synthetic molecules behave differently in nano-confinemnets owing to forces such as charge and surface energy that become dominant at nanoscale. Nanoscale devices offer high throughput, sensitivity and selectivity with low sample volume and concentrations.

## 1.1 Major Objective

The main purpose of this work is to design and fabricate devices operating at nanoscale to increase the assay sensitivity and decrease the cost of current molecular diagnostic tools.

## 1.2 Overview of Research Work

This research describes the fabrication and application or phenomenon in five devices. An in-depth literature review covering current diagnostic devices, their limitations, state of art to fabricate microfluidic channels and self assembly of organo-silane is done in chapter 2. Chapter 3 details the fabrication, application and results of using nano-junctions to detect DNA mutation. Chapter 4 covers the fabrication and use of functionalized nanochannels to purify proteins from

1

mixtures. Chapter 5 covers the effect of fluorescent dyes on fluid flow through nanochannels. Chapter 6 delves into fabrication of aligned microchannels in polydimethylsiloxane (PDMS) using novel techniques. The proposals for future are detailed in last chapter.

Following is the overview of devices described in detail in later chapters.

### 1.2.1    DNA detection

In this study, a specific DNA target sequence was electrical detected using an engineered DNA probe. Hairpin probe DNA was immobilized on silicon chip between gold nano-electrodes. Hairpin DNA are thermodynamically very stable and open up only upon complete hybridization of the loop sequence. This hairpin is critically designed to respond only to the presence of mutated sequence. A reporter sequence carrying gold nanoparticles detects hairpin opening, by hybridizing with the stem region of opened hairpin. Nanoparticles result in increased charge conduction between nano-electrodes. An 18 base long segment of *K-Ras* oncogene was used as a model sequence and electrical measurements were done across nanoelectrodes to detect femto-level concentration of target sequence.

### 1.2.2    Active filtration of proteins

A device was introduced that used unique interaction of antigen-antibody in nano-confinements/nanochannels to keep check on the molecule passing through it. These were polycarbonate channels functionalized with different antibodies that selectively filtered corresponding antigen from a pool of molecules. These devices can increase the signal-to-noise ratio for target molecule in sample, and thus can effectively be used as pre-filtration devices for low abundant biomarker sample detection.

### 1.2.3  Effect of fluorescence in nanoconfinements

Conjugation of fluorescent tag to protein molecules was seen to have critical effect on filtration of protein through nanochannels.  Tagging of protein with one kind of dye enhances its flux through channels owing to complex charge, shape and other forces dominant at nanoscale.

### 1.2.4  Self-aligned PDMS channels

In this study, few simple and cost-effective approaches using bench-top tools to fabricate aligned microchannels and PDMS membranes were demonstrated. Because it employed the use of simple materials like nanoparticles, magnets, polycarbonate beads and acetone, the technology can be executed with minimal need for special facilities. The principle behind this fabrication is that the PDMS is hydrophobic and directional polymerization of polymer 'kicks' out the hydrophilic material due to phase separation leaving behind a trail of track in the form of empty channel.

CHAPTER 2

BACKGROUND AND LITERATURE REVIEW

## 2.1 Diagnostics

A major need in disease diagnosis is the detection of low abundant secretory and tissue leakage protein biomarkers. Current immunoassays have high throughput and selectivity. Some of the assays such as radioimmuno assay (RIA) are very sensitivity but associated with high cost and expertise. On the other hand, low end assays are cheaper and easy to handle but marred by lower assay sensitivity.

### 2.1.1 Current Immunoassays and factors associated with choice of assay

Advancements in diagnostic techniques provide analysis tools for complex samples with sensitivities down to single molecule. However, the associated complexity and cost prohib the mass usage of such sophisticated tools. Various immunoassays like precipitation reaction, agglutination, turbidometry and immunofluorescence can inexpensively detect the target antigen in range of 2-200 µg/ml. For low antigen concentration, flow cytometry, enzyme linkied immunosorbant assay (ELISA) and RIA can be used that can sense down to .006 µg/ml of target antigen concentration[1]. These techniques require certain level of expertise setting up and operating the equipment. Further, the selection of methodology is dependent on concentration of analyte, epitope density, and molecule size. Radioisotopes for RIA are restricted by legislation in many countries across the globe. Restriction of patents constrains the availability of reagents for technologies like time-resolved fluorescence, enzyme amplification by co-factor cycling and enhanced chemiluminescence. Better separation/purification techniques are required to increase the signal-to-noise ratio.

*2.1.2  Sample purification and device sensitivity*

Biospecimens are primarily complex mixtures of various biomolecule which cause high background noise for any analytical technique. Sophisticated techniques like mass spectroscopy, MALDI-TOF or surface plasmon resonance can profile and detect low concentration of proteins but demand high signal-to-noise-ratio as well. For all these techniques, a suitable matrix/control that mimics the behavior of the sample matrix is required. If the exact composition of the sample is known an analyte free matrix can be synthesized. But, for complex matrices, like serum generally matrix from same species is employs which is not the true background and decrease the assay sensitivity.  Effective separation of molecules based on physico-chemical properties is critical to increase the dynamic range of detection. The use of separation steps for complex samples (or heterogeneous mixtures) gives more specificity, better precision and sensitivity. Some of separation techniques currently used include electrophoretic separation, chromatography, surface adsorption, fractional precipitation, solid phase separation, entrapping and microencapsulation[1].   In an ideal separation technique, the sample equilibrium should not be perturbed, there should be minimal non-specific binding, negligible sample-matrix interaction, and it should provide rapid results within reasonable cost. Table 2.1 shows some of the current separation techniques and limitation associated with them.

*2.1.3 Purification through nanochannels*

Nanostructured membranes have been shown to separate several chemical moieties. Separation through nanoporous is based on differences in target physicochemical properties, like charge, size [2, 3], hydrophobicity [4], and isoelectric point [5]. These approaches can efficiently separate target molecule from defined mixture of molecules (i.e., molecules in mixture are known), but may not be suitable for selectively filtering target molecule from undefined biospecimens such as blood plasma or urine with unknown molecule properties.

Table 2.1. Current separation methods and limitations

| Method | Limitations |
|---|---|
| RIA | • Require high specific active radioisoptope eg I$^{131}$ |
| SDS-PAGE | • Loss of native conformation of protein due to SDS |
| Isoelectric focusing | • Proteins with similar pI values but very different sizes can run at the same position |
| Immunoblotting | • Include protein adsorption on membrane ; doesn't work good for hydrophobic proteins<br>• Need multiple step blocking and washing to reduce false positive signal<br>• Uses labeled secondary antibodies<br>• Have to revive analyte after separation<br>• Time consuming |
| Size exclusion chromatography | • Molecules of similar size elute in single fraction<br>• Not used to separate complex mixture like serum containing invariable antibodies and proteins of similar size |
| HPLC and TLC | • Separation based on size, charge and hydrophobicity<br>• Sophisticated instrument but needs expertise and not used regular due to associated cost |
| Adsorption | • Batch to batch variation<br>• Not suitable for complex biological fluids such as serum |
| Fractional precipitation of proteins | • Often done using ethanol, ammonium sulfate and PEG<br>• Require high concentration and volume of target analyte |
| Solid phase separation | • Generally used for non-specific separation |
| Polymerization | • Partial loss of immunoreactivity of antibodies following polymerization |

*2.1.4 DNA Sensors*

Microarrays are a common method used to screen genetic material for the presence or absence of particular genomic sequences. Microarrays use single stranded DNA probes attached to a silicon chip and fluorescently tagged genomic DNA is hybridized to the probe. The fluorescent markers are excited for detection. Fluorescent tags, however, can affect the stability

and fidelity of the probe-target interactions—reducing reliability [6].  To overcome these limitation several  experiments  have demonstrated the potential of hairpin probes to improve reliability and fidelity of microarrays. In addition, a number of alternative detection mechanisms have been reported with the detection limits between 1.8 and 10 fmol  [7-9]: impedance measurements [10], capacitance detection [11], cyclic voltammeter measurements [12], and calorimetric measurements.

## 2.2 Micro-channels

Soft lithography has become a method of choice to make microfluidic channels.  In most of the soft lithography approaches, hard masks are made of SU-8 polymers using optical, electron-beam or ion-beam lithography.   Hard  masks  are  then  used  to  mold  elastomer materials.  Small channels or structures are made routinely using silicon elastomer and hard masks. These dimensions leads to high heat transfer coefficient, pressure drops and laminar fluid flow. These microfluidic channels are used for biosensor application[13], separation of biomolecule and chemicals [14], fuel cells[15]  etc.

In most applications molds for microfluidic channels are made by producing a master pattern in photoresist on the surface of the silicon wafer by photo- or e-beam lithography (EBL). The liquid elastomer is poured over it and cured into the rubbery solid. The elastomer stamp is then peeled off the master.  The fabrication of the master is expensive due to use of the EBL or other advanced techniques.

### 2.2.1    PDMS properties

Polydimethylsiloxane (PDMS) is an organosilicon compound typically used to make microfluidic channels.  PDMS is hemocompatible/biocompatible [16] and have been found to be non-toxic for bio-applications.  It has shear elastic modulus of G ~ 250 kPa, high resistance to change in shear elasticity with change in temperature (1.1 kPa/ºC) and low glass transition temperature of 125 ºC [17]. It is transparent, can sustain high temperatures and has biologically

7

relevant Young's Modulus [18]. PDMS is used to make microfluidic biological sensors, fuel cells and on-chip DNA amplification systems. PDMS membranes are manufactured for use in pervaporation experiments to remove organics, as soft elastic substrates to study cell movement, for cell adhesion and for aligned microfluidic [19-21]

### 2.2.2 Soft lithography

Photolithography is an established technology in silicon industry. It is used to transfer chip designs on silicon wafers. Optical lithography uses light to transfer a geometric pattern from a photo mask to a light-sensitive chemical on the substrate. Series of chemical treatments lead to pattern formation on the wafer.

In soft lithography, the PDMS is polymerized over the processed wafer from photolithography, called 'master' and patterns are transferred to polymer, called 'stamp'. These stamps are used in different techniques to transfer patterns on surfaces. Soft lithography is high throughput but expensive due to photolithography involved in the overall process. Some of the disadvantages are: (i) Shrinkage of polymer during curing. (ii) Swelling by non-polar solvents, (iii) Sagging and deformation [22].

### 2.2.3 Micro-channels fabrication

Various methods are used to fabricate microfluidic devices with varying channel sizes and multilevel channel structures like multilayer lithography [23-25], laser micromachining [26], electron beam lithography [27], object printing [28], reaction–diffusion [29] and synchrotron radiation technique [30]. Other techniques are used to make hard multilayer resist patterns for microfluidic device in glass, silicon and biopolymers [31]. All these methods are expensive and require sophisticated equipment and clean room environment. As an alternative, inexpensive methods that uses nylon fiber [32] and low surface energy templates [33] have been recently reported. However, removal of nylon templates requires organic solvent that result in PDMS swelling and low energy templates are limited in their dimensions. Simple porous structure in size range of 4-6 μm using water as porogen has been reported [34] and used as pH sensor.

8

CHAPTER 3

ELECTRICAL DETECTION OF MUTATION IN ss-DNA


This chapter covers the details of DNA designing, chip fabrication, functionalization of DNA on silicon surface and experimental set-up and details of the target reorganization and electrical measurements.


## 3.1 Hairpin Design of probe DNA

DNA can take up variable secondary structure/shapes such as dimmers, loops and bridges depending upon its chemical environment. One such special structure is hairpin loop DNA where two extremities of DNA are complementary to each other and tend to stick together below the $T_m$ to form a hairpin structure. Figure 3.1 shows formation of hairpin structure from open confirmation where red and green parts are complementary to each other.
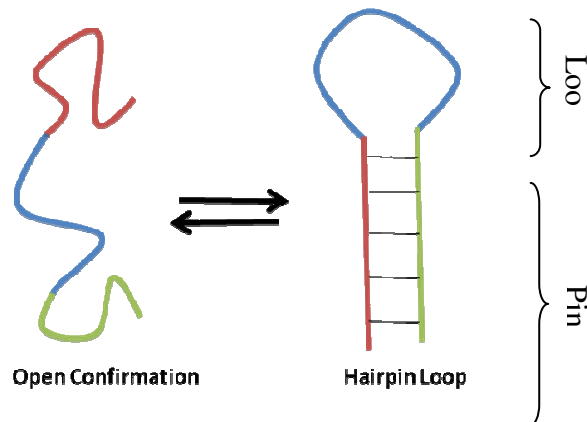


Figure 3.1. Secondary structure (hairpin) confirmation of DNA.

These loops are thermodynamically very stable and unwind only at high temperature or in presence of DNA which is complementary to complete looparea and at least one part of the loop region as demonstrated by several studies [72-74]. We designed hairpin probe DNA to respond specifically to mutated target DNA. The DNA oligonucleotides used in this study, Table 3.1, were purchased from Sigma Aldrich (Saint Louis, MO).

Table 3.1. DNA sequences and their modifications

| Sequence Name | Oligonucleotide (5' to 3') | Modification |
|---|---|---|
| Hairpin Probe | AAAGGCAATTTCGCCGCCGCCATTGCC | 5' C12 Amine |
| PC-target | GGC A**A**T GGC GGC GGC GAA | None |
| MM-target | GGC A**G**T GGC GGC GGC GAA | None |
| GNP-reporter | TGCCTTT | 5'Thiol and GNP |

The oligonucleotides are given the names "hairpin probe," "PC-target," "MM-target," and "GNP-reporter" based on their role. Hairpin probe oligonucleotide consisted of a three nucleotide spacer, a twelve nucleotide loop, and a six base pair stem. The target oligonucleotides, PC-target and MM-target, were identical to each other except at one position (marked in bold in Table 3.1). PC-target was perfect complementary to the loop plus a portion of the stem of the hairpin probe. MM-target is the 18 bp wild type DNA taken from *K-ras* oncogene (accession number NM_033360, bases 31-40 (5'→3')). The probe was designed to be complementary to PC-target to detect the mutation; therefore, the MM-target/wild type DNA was unable to open and hybridize the hairpin probe while PC-target opened the hairpin structure and forms a duplex, shown in Figure 3.2.

10
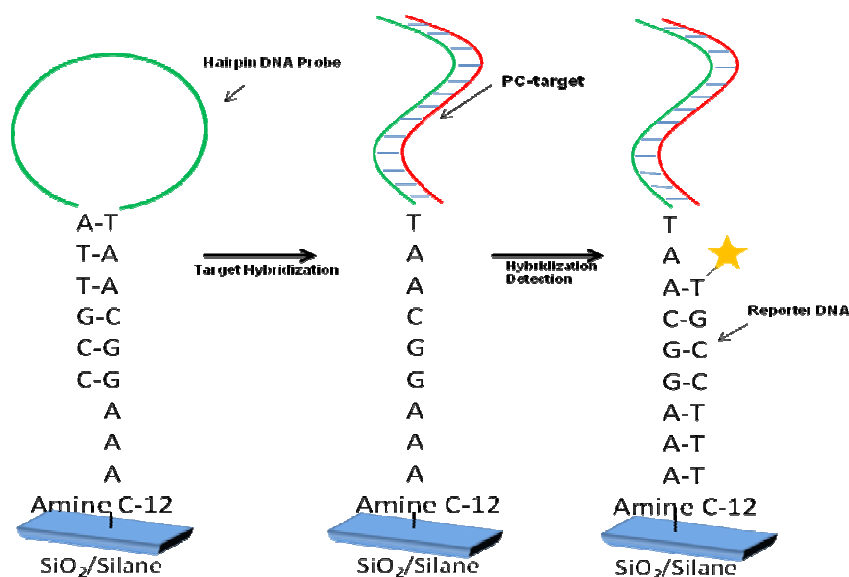
Figure 3.2. Schematics showing reporter sequence carrying the gold nanoparticle (yellow star) binds to probe when the hairpin is opened by PC-target DNA (red).

The seven base reporter DNA, GNP-reporter, increases the detection limit of the system by increasing electrical conductance across the nano-electrodes when the hairpin is in the open configuration.

## 3.2. Surface chemistry

For the surface attachment of probe DNA, the chips were cleaned in oxygen plasma at 200 W in $Ar+O_2$. This treatment also made the surface hydrophilic. Surface functionalization of the chips was done in a nitrogen glove box with controlled ambience and temperature, as previously reported [72]. Once attached, the probe molecule was heat-cycled in TE (Tris-EDTA) buffer 3 times to ensure all molecules formed hairpin loop structures. The GNP-reporter conjugates were prepared using thiol-gold chemistry [75]. The functionalized chips were immersed in buffer (pH 7.4) containing target DNA, either PC-target or MM-target, at different concentration of target DNA solutions for 24 hours at 40 ˚C, followed by rinse with methanol and deionized water. Chips were then incubated in buffer solution containing GNP-reporter. The

11

reporter-sequence binds to the stem region of the probe towards the chip surface when it becomes available on binding of PC with probe (and is unavailable otherwise). In addition to the "PC" and "MM" chips, two control chips were used: (1) Chips with probe DNA but not exposed to any target DNA; (2) chips without probe molecule not exposed to target DNA (only the silane SAM surface chemistry). Control chips were incubated with GNP-reporter sequence as above. Neither control chip showed reactivity with or attachment of the GNP-reporter sequence.

The covalent and electrostatic attachment of DNA on silicon chip was tested using two types of buffer tris-EDTA and tris-DIPE to increase probe density of substrate. Acridine orange dye was used to detect the presence of DNA on surface. For this the chips were incubated in 20mM solution of dye for 15 min and rinsed with DI water thrice to remove the excess dye on the surface. Acridine orange is a nucleic acid specific dye that intercalates in-between the DNA bases For double stranded DNA, its emission is at 525 nm and for single strand DNA/RNA the emission wavelength is 650nm. Image analysis was done using *Image J.*

### 3.3    Device Design and Data recording

The device consists of fabrication of Au electrodes separated by 500 nm apart shown in Figure 3.3.
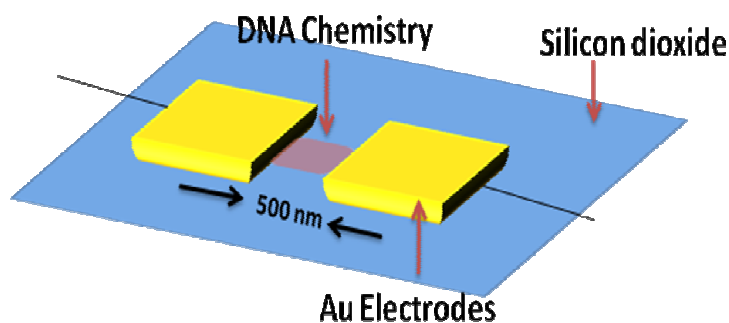


Figure 3.3. Device Design for DNA detection

The number of GNPs on the surface of control, MM, and PC bare silicone chips was visualized by scanning electron microscopy (SEM) and manually counted using *ImageJ* software [76]. For electrical measurements, probing of control, MM, and PC nano-electrode chips was done using Agilent 4155C semiconductor parameter analyzer with a sweep of -1 V to 1 V.

**3.4      Results**

The attachment chemistry and overall design was verified at different stages.

*3.4.1   DNA attachment on surface*

The concentration of oligos attached via covlent bond between PDITC and NH2 was 1 fold higher for Tris-DIPE and 2.5 folder higher in TE buffer pH 7.4 than oligos attached via electrostatic bond between positive charge on surface amine group and negative charge on oligo backbone. They were statistically different with p value of 0.00046 for tris-EDTA and 0.0047 for tris-DIPE.  Diisopropylethylamine (DIPE) is a non-nucleophillic organic base that accelerated the reaction of amine with thiocynate without forming tertiary compounds.



|        (a)         |        (b)         |
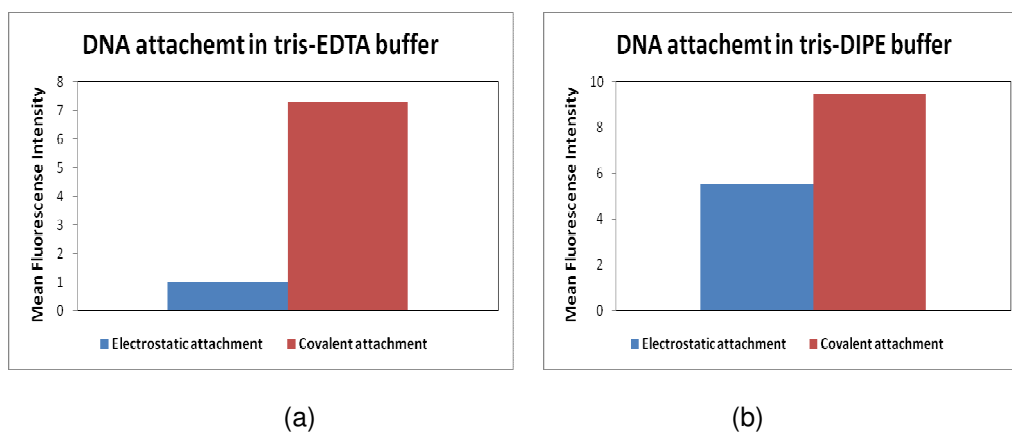
Figure 3.4. DNA attachment (a ) TE buffer (b)  tris-DIPE buffer

<div align="center">(a)            (b)</div>
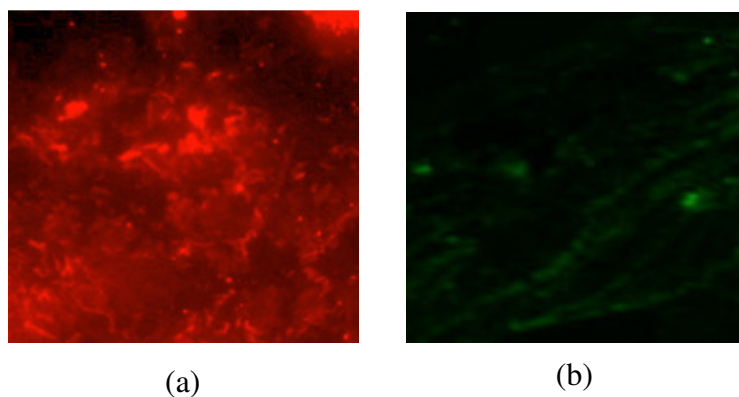
Figure 3.5. Fluorescent images of DNA on silicon surface. (a) ss-DNA (b) ds-DNA

Figure 3.4 shows the plot of DNA attached on the surface in different conditions. Figure 3.5 shows the fluorescence images on DNA attached on the surface. The brightest area was considered while recording fluorescent value using *Image J.*

*3.4.2 Microscopic Analysis*

The presence of GNP on surface was analyzed by SEM. The densest area was selected for micrographs. The attachment of PC- DNA on surface corresponded to attachment of reporter DNA with gold-nanoparticel (GNP). In Figure 3.6, GNPs are visible as white dots. Left image shows chip with Probe, PC-target and GNP-reporter. Right image shows chip with Probe, MM-target and GNP-reporter. The data clearly demonstrated the selectivity of probe to bind with PC DNA.



<div align="center">(a)            (b)</div>
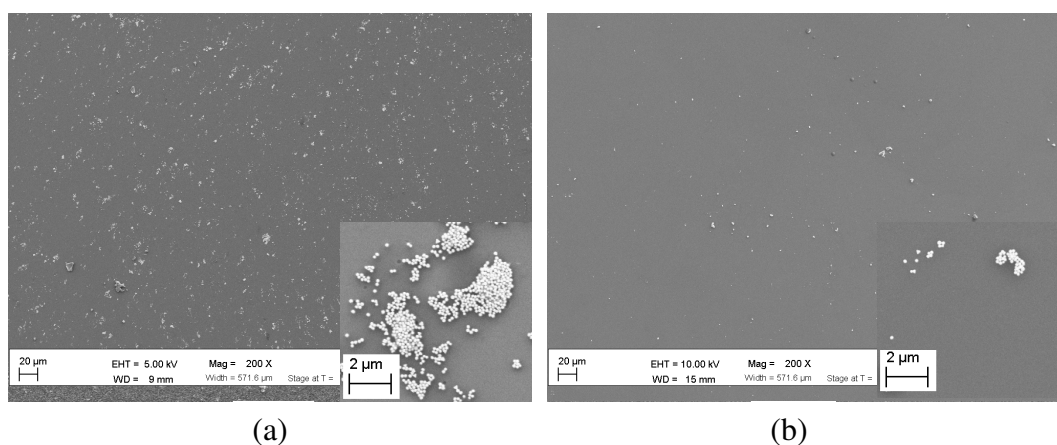
Figure 3.6. SEM micrograph showing (a) GNP attachment corresponding to PC-DNA hybridization (b) significantly less number of GNP for MM-DNA

The nanoparticle counts were normalized as number of GNPs per square micron as shown in Table 3.2

Table 3.2. Count of average number of GNPs on silicon surfaces

| DNA Complexes | Mean # of Particles/$\mu m^2$ | St. Dev. |
|---|---|---|
| Hairpin Probe+PC-target+GNP-reporter | 11.62 | 5.60 |
| Hairpin Probe +MM-target +GNP-reporter | 0.86 | 0.76 |
| Hairpin Probe+GNP-reporter | 0.10 | 0.09 |
| GNP | 0.01 | 0.00 |

The counts showed 10 time difference in number of GNPs captured by the probe in case of PC-target than for MM-target, and negligible number for control chips. Figure 3.7 shows the graphical representation of number of particles present per $\mu m^2$. The data label shows the type of DNA/chemical involved in each attachment.
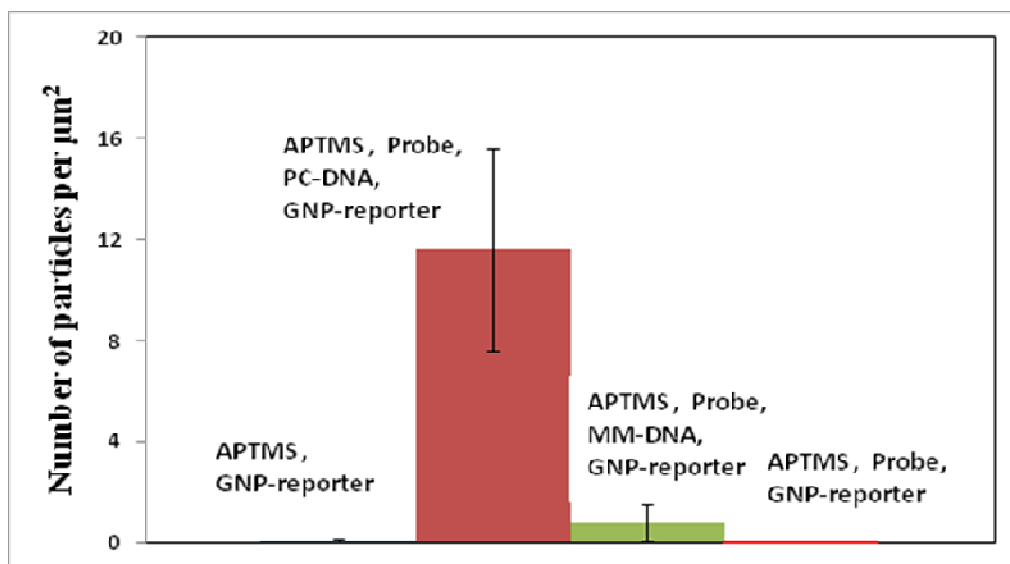


Figure 3.7. Graphical representation of number of particles present per micrometer square of silicon wafer
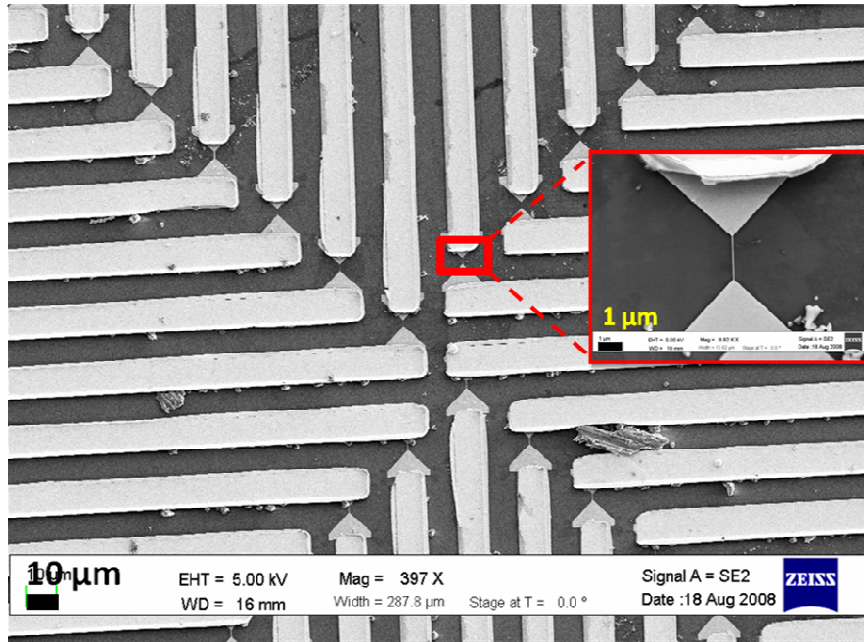
(a)
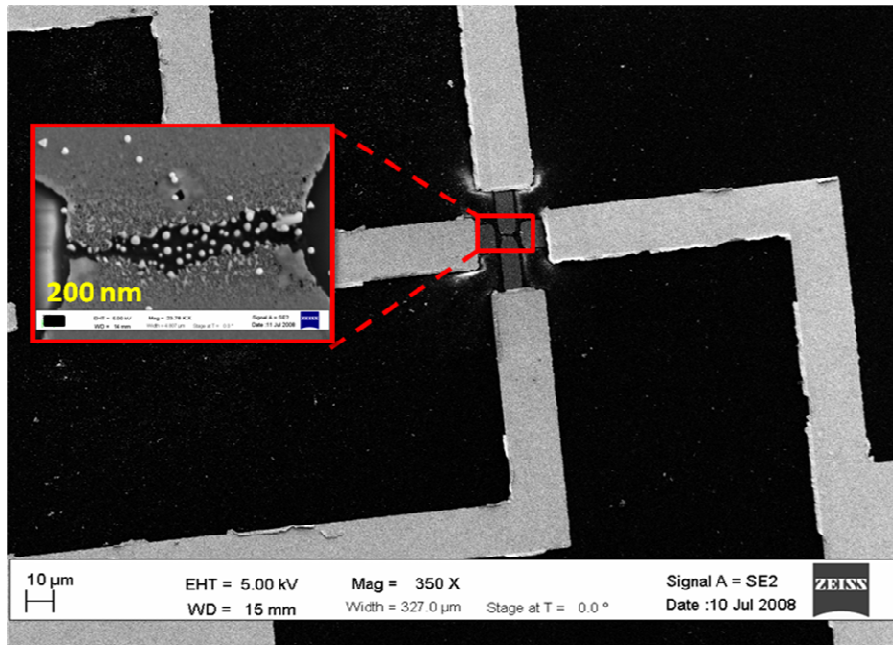


(b)

Figure 3.8. SEM micrographs of nanoelectrodes chips

16

Different devices used for DNA detection is shown in Figure 3.8. The micrograph in Figure 3.9 show nano-electrode chips after DNA run. The GNP density on MM-target chip is significantly lower than the GNP density of PC-target chips.



(a)                                                                      (b)
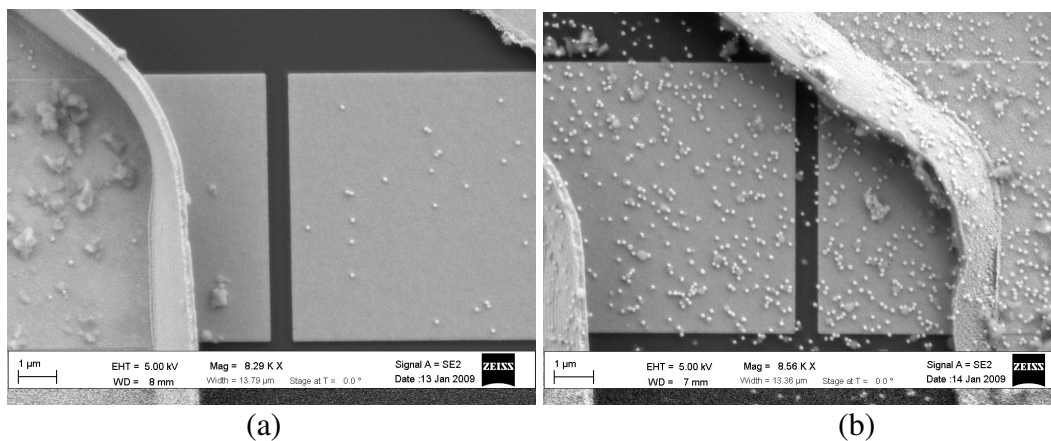
Figure 3.9. SEM micrographs of nano-electrode chips. The SEM micrographs show a distinct difference in the GNP densities on (a) MM-target chips and (b) PC-target chips

### 3.4.3   Electrical Measurement

The electrical conduction was measured through the nanoelectrodes before and after DNA attachment. Presence of GNP corresponding to presence of target PC-DNA showed increase in the current across gaps due to hopping of electron from one GNP to another. The *I-V* measurements for MM-DNA chips revealed around 3% of the nano-electrode pairs showing slight increase in conductivity (within same order). More than 70% of nano-electrode pairs for PC-chips showed robust increase in conductivity. For PC chips, *I-V* measurements showed six orders of reduction in the resistance between the nano-electrodes measured between -1 to +1 V in the presence of the GNP-reporter. Figure 3.10 shows representative measurement of *I-V* data before and after target DNA attachment.

17
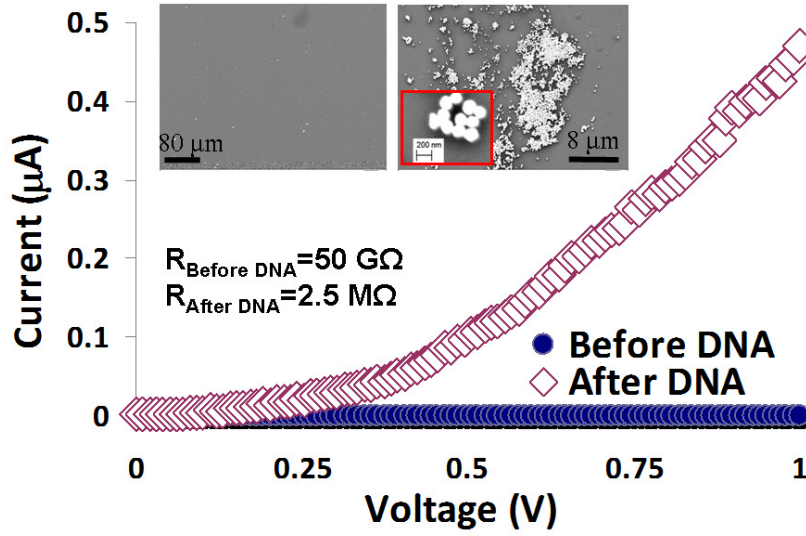
Figure 3.10. Comparison of *I-V* characteristic of nanogap before and after exposure to PC-target and GNP-reporter.

Blue dots show current before hybridization of PC-target with surface bound probe. Red diamonds represent the *I-V* data after hybridization of PC-DNA and GNP-reporter.

## 3.5 Discussion

We used a hairpin based probe located between nano-electrodes to which a gold-nanoparticle (GNP) conjugated oligonucleotide was engineered to act as an efficient reporter of probe-target hybridization.

The presence of GNPs provides charge hopping sites to carriers thus acting as transduction and amplification block indicating the binding of PC with the probe. The tunneling current in a system of the nano-gap electrodes with insulator (vacuum) between them can be approximately described by Simmons formula [77]:

$$J = \frac{\alpha}{\delta_z^2} \left\{ \overline{\varphi} \exp\left(-A\delta_z \sqrt{\overline{\varphi}}\right) - \left(\overline{\varphi} + eV\right) \exp\left[-A\delta_z \sqrt{\overline{\varphi} + eV}\right] \right\}$$

where $\alpha = e/4\pi^2\beta^2\hbar$, $A = 2\beta\sqrt{\frac{2m}{\hbar^2}}$, $\overline{\varphi}$ is average barrier height relative to Fermi level of the negative electrode, $\delta_z$ is barrier width and $eV$ is applied bias energy (voltage) between the

18

electrodes. The term $\beta$ is dimensionless correction factor, $e$ and $m$ are charge and mass of electron respectively, and $\hbar$ is Dirac's constant. At small voltages when $\bar{\varphi} << $ eV, the Simmons formula simplifies as $J = \frac{\gamma\sqrt{\bar{\varphi}V}}{\delta_z}\exp\left(-A\delta_z\sqrt{\bar{\varphi}}\right)$, where $\gamma = \frac{e\sqrt{2m}}{4\beta\pi^2\hbar^2}$. In this case $\bar{\varphi}$ does not depend on the applied voltage $V$ between the electrodes so the tunneling current becomes proportional only to $V$. The tunneling current characteristic can thus be modeled as two electrodes with high resistance between them. As the PC-target binds between these electrodes and GNP-reporter brings in GNPs, electrons find a lower barrier and thus start tunneling efficiently. Such framework can act in a similar fashion as microarrays with electrical conductivity as the detection factor.

Subsequent SEM imaging of the MM and PC nano-electrode chips confirmed the validity of the *I-V* measurements (Figure 3.9). The images showed clusters of GNPs on PC-target chips between the nano-electrodes which provided the pathways for increased current through otherwise insulating electrodes. SEM micrographs also showed negligible number of GNPs on the surface of MM-DNA chips. The few GNPs on the MM chips can be attributed to physical adsorption. This clearly shows inability of MM-DNA to open the probe hairpin loop, resulting in little or no GNP-reporter attachment.


**3.6 Conclusion**

In summary, we presented that the single base mis-match in DNA can be detected by hairpin probe specificity. The hybridization can be probed using GNP-reporter sequence complementary to stem region of hairpin, which open up on perfect hybridization with complementary sequence. Presence of GNP between electrodes enhanced the DC current that can be mapped back to the presence of mutation in target sample. The device can do what microarrays do at concentrations of as low as femtomoles, but without the need to tag the probe

or target molecules.  The GNP-reporter can be modeled as a circuit breaker demonstrating

interactions of molecules can be quantified electrically.

CHAPTER 4

ACTIVE FILTER TO PURIFY PROTEIN MOLECULES THROUGH NANOCHANNELS

Selective protein channels in cell and nuclear membrane act as gateways to control the passage of molecules across the junction. The selectivity of these channels stem from attractive potential generated by transmembrane proteins and channel dimension in nanometer. They can filter out small volume of solutions with high precision. Based on the same phenomenon, here, we report biomimetic facilitated transport modality to selectively separate a target molecule (BSA or Hb) from its mixture.  Anti-BSA and anit-Hb antibodies are used to create attractive potential inside the nanochannel.

**4.1 Device Fabrication**

Polycarbonate membranes  with 15 nm diameter nanochannels were activated using UV/Ozone plasma for 220 seconds with shiny side facing up. For PDMS casting, Sylgard 184 was mixed in 10:1 ratio and polymerized at 110 ˚C for 4 hours.  The holes of 6 mm diameter were made using biopsy punch. Two layers of PDMS were aligned and membrane was sealed in between using Sylgard 184 in ratio 20:1 and left overnight at room temperature. The membranes were 6 μm thick with nanochannel density of $6X10^8$ channels/cm$^2$. The effective filtration area was 110 mm$^2$. The schematic is shown in Figure 4.1.

Carboxyl groups were generated using oxygen plasma. Either anti-BSA or anti-Hb antibody (2mg/ml) was diluted 1:500 in PBS with 20 mM 1-ethyl-3-(3-dimethylaminopropyl) carbodiimide (EDC) and 10 mM *N*-Hydroxysuccinimide (NHS) (Sigma, Saint Louis). The antibody solution was applied on the upper side of the device (UV activated surface) and

incubated at 4 °C for overnight. The devices were then washed with copious amount of PBS, and incubated with 4% goat serum in PBS for one hour to block unreacted carboxyl groups and decrease the non-specific protein adsorption.  It was then washed vigorously and used for filtration.
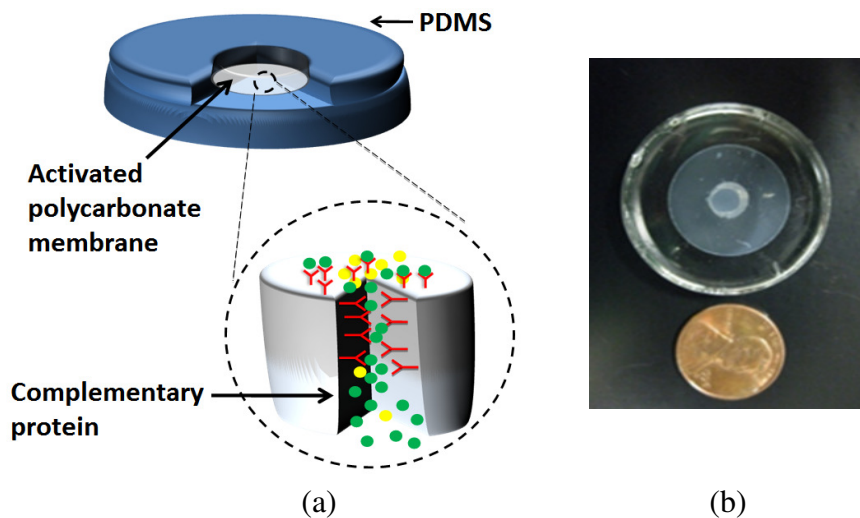


Figure  4.1. (a) Schematic of active filtration device.  The red Y-shape antibody interacts specifically with green molecule and enhances its flow across the nanochannel (b) Top view of PDMS device

## 4.2 Selective Filtration of Proteins

The separation of protein was carried out in two set of experiments, with four independent devices in each set. One set was immobilized with anti-BSA antibodies; the other set was immobilized with anti-Hb antibody. For filtration, the mixture of BSA and Hb (1 µg/µl) protein solution was added on the activated side of the device, and 80 µl of PBS (pH 7.4) was added on the other side.  8 µl of PBS containing filtered molecules was collected as sample after every 30 minutes. In other experiments BSA ratio was increased to 20 and 40 times, while keeping the Hb concentration at 1 µg/µl to defer the effect of increased BSA on Hb filtration through anti-Hb immobilized devices. The concentration of BSA and Hb was quantified by measurement of absorption at 278 nm and 408 nm respectively using Nanodrop UV-Vis

Spectrophotometer (Nanodrop Technologies, Wilmington, USA).  For control experiment, the devices without antibody immobilization are used to filter BSA and Hb mixture.

## 4.3 Statistical Analysis

We considered a mixed-effects model for our data analysis.  The factor of protein was modeled as fixed effect because we were interested only in the BSA and/or Hb selected for study and did not make inferences about other proteins.  The factor of device was included as random effect in the model considering the device representative of a larger population of devices of interest.  Both fixed and random effects constructed our mixed-effects model as:

$y_{ijk} = \mu + \alpha_i + \tau_j + \beta \cdot t_{ijk} + e_{ijk}$ , where $i$ = 1, 2,  $j$ = 1,...,4, and $k$ = 1, ..., 6.  Here $\alpha_i$ is the fixed effect of protein $i$, $\tau_j$ is the random effect of device $j$, and $t_{ijk}$ is the continuous variable of time and $e_{ijk}$ is the random error associated with the $k^{th}$ observation from the $i^{th}$ protein and $j^{th}$ device.  The distributions of $\tau_j$ and $e_{ijk}$ are normal with zero means $\tau_j \sim$N(0, $\sigma_v^2$) and $e_{ijk} \sim$N(0, $\sigma_e^2$), where $\sigma_v^2$ and $\sigma_e^2$ denote the variances of $\tau_j$ and $e_{ijk}$, and $\tau_j$'s are independent of the $e_{ijk}$, and of each other.  We tested the null hypothesis in our analysis i.e. H$_0$: $\alpha_1 = \alpha_2$, that is to say that there was no difference between the measure of the concentration of the first and second protein in the sample.  The procedure of PROC MIXED in SAS version 9.1 was employed to conduct the analysis with the restriction of $\alpha_2$ = 0.

## 4.4   Results

The proteins were measured spectroscopically on other side of membrane. The BSA and Hb absorbtion was recorded at 278 nm and 408 nm respectively.

*4.4.1 Antibody attachment on polycarbonate membranes*

Attachment chemistry for surface immobilization of antibody using carbodimide reaction was confirmed using Alexa 488 tagged goat anti-rabbit antibody. Figure 4.2 shows the comparison of antibody attachment using carbodiimide chemistry on plasma oxidized polycarbonate membrane and native membrane. Therefore, plasma oxidation to generate oxide groups and EDC chemistry is critical to antibody attachment.
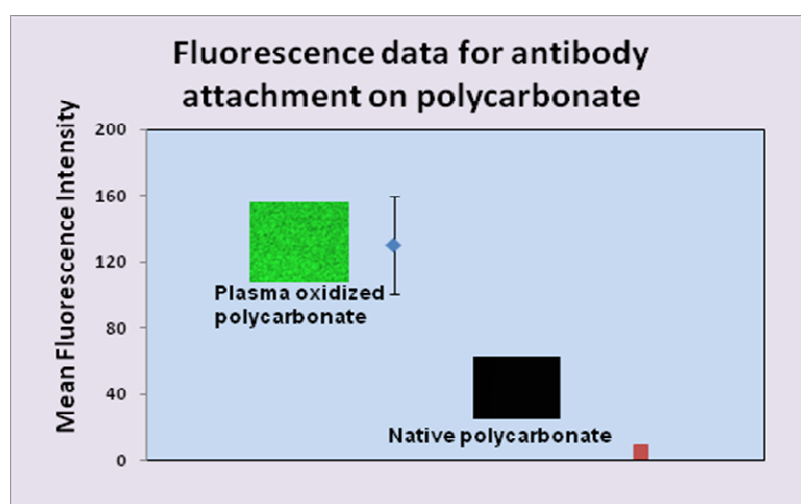


Figure 4.2. Fluorescence data on antibody attachment on plasma oxidized polycarbonate membrane and native membrane

*4.4.2    Protein  selectivity through channels*

For control experiment, slightly higher flux of BSA ($6.887 \times 10^{-4}$ µM/min) than Hb ($2.2693 \times 10^{-4}$ µM/min) was observed at pH 7.4 despite their similarity in physicochemical properties (Figure 4.3). The data is average readings collected from four independent devices (n=4) and error bars are standard deviation. The x-axis is the time for sample collection and y-axis is concentration of respective filtered antigens. The flux of BSA across membrane was $6.887 \times 10^{-4}$ µM/min and the flux of Hb was $2.269 \times 10^{-4}$ µM/min. These numbers, which depict the molecules translocated in the absence of antibodies, were taken as baseline to evaluate the

actual number and ratio of molecules translocated in the presence of antibodies in functionalized membranes.  Separation factor $\gamma$ is the ratio of flux of BSA to the flux of Hb, and separation factor $\beta$ is the ratio of flux of Hb to the flux of BSA.
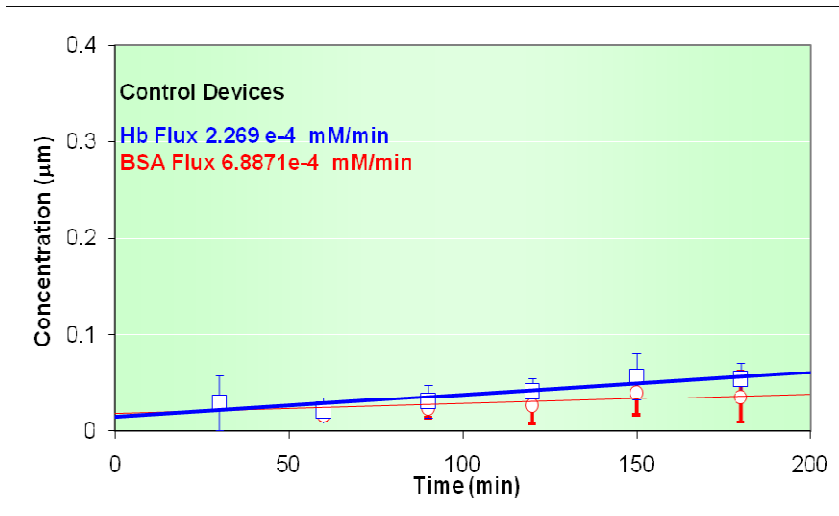


Figure  4.3.  Comparison of amount of molecules transported in non-functionalized native membranes used as control.

Table 4.1. Permeation data and separation factor for control and functionalized (BSA:Hb=1:1)

| Functionalization | Transport rate of molecules (µM/min) | | Separation factor | |
|---|---|---|---|---|
| | BSA | Hb | γ | β |
| Control | 6.8871e-4 | 2.2693e-4 | **3** | **0.33** |
| Anti-BSA antibody | 1.2608e-3 | 2.2941e-4 | **5.2** | 0.18 |
| Anti-Hb antibody | 3.0281e-3 | 3.9831e-3 | 0.65 | **1.5** |

For devices functionalized with anti-BSA antibodies, the mixture of BSA and Hb solution was allowed to filter through the activated side. It was observed that the flux of BSA in functionalized membrane was significantly increased (1.8 times) as compared to the flux of BSA in control device. However, the flux of Hb remained same as that in control device (Table

4.1, Figure 4.4(b)). The separation factor $\gamma$ (ratio of *flux of BSA to Hb*) for anti-BSA antibody functionalized devices increased to 5.2 as compared to $\gamma$ of 3 for control device.
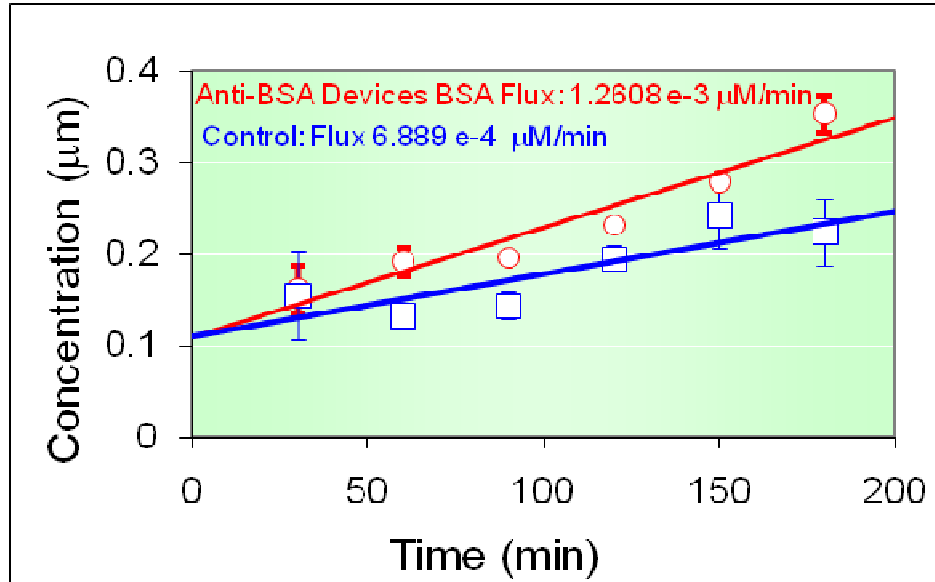


(a)
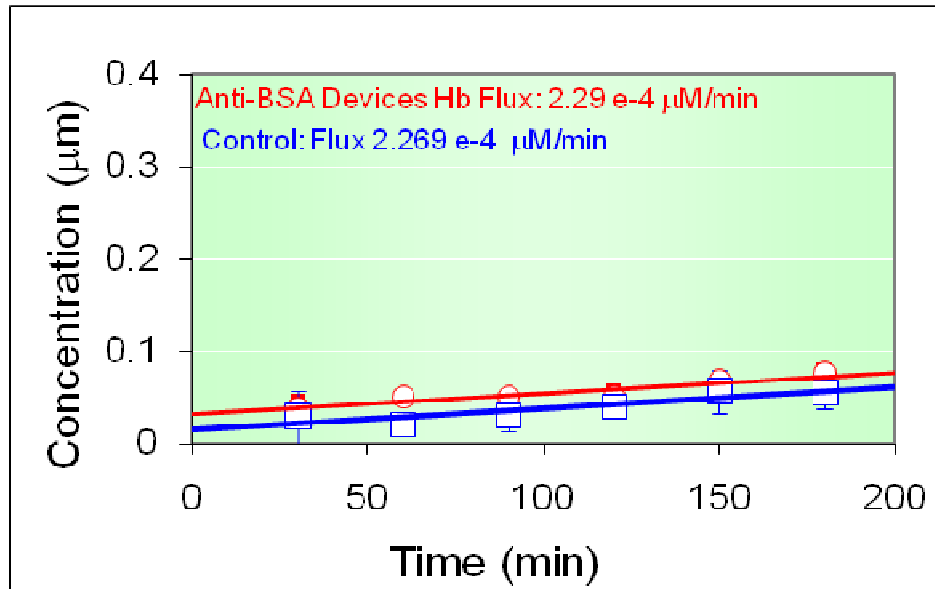


(b)

Figure 4.4. Molecules translocated through anti-BSA antibody functionalized membrane. (a) Comparison of BSA transport through anti-BSA antibody functionalized and non-functionalized native membrane. (b) Shows the comparison of Hb transport through anti-BSA antibody functionalized and non-functionalized native membrane. (n=4)
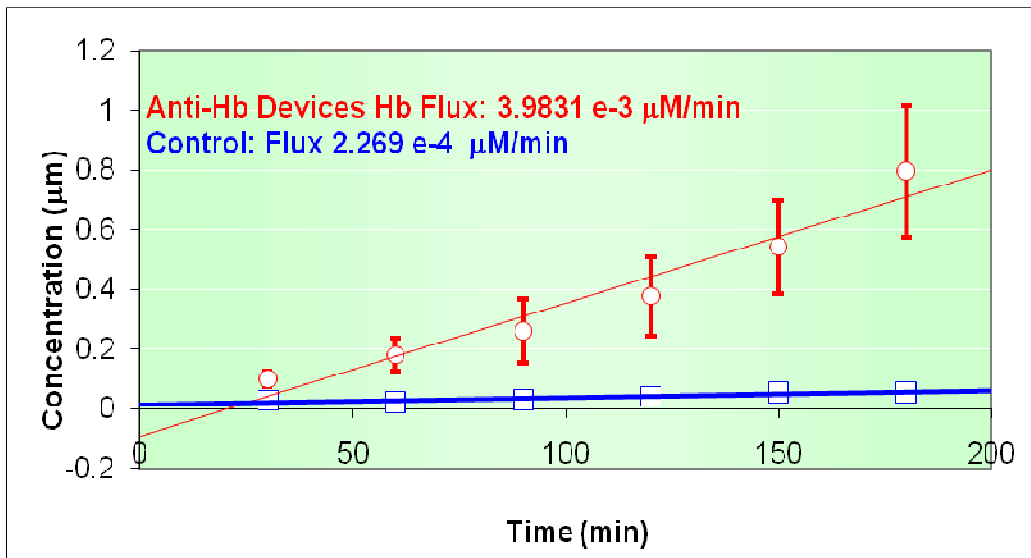
(a)
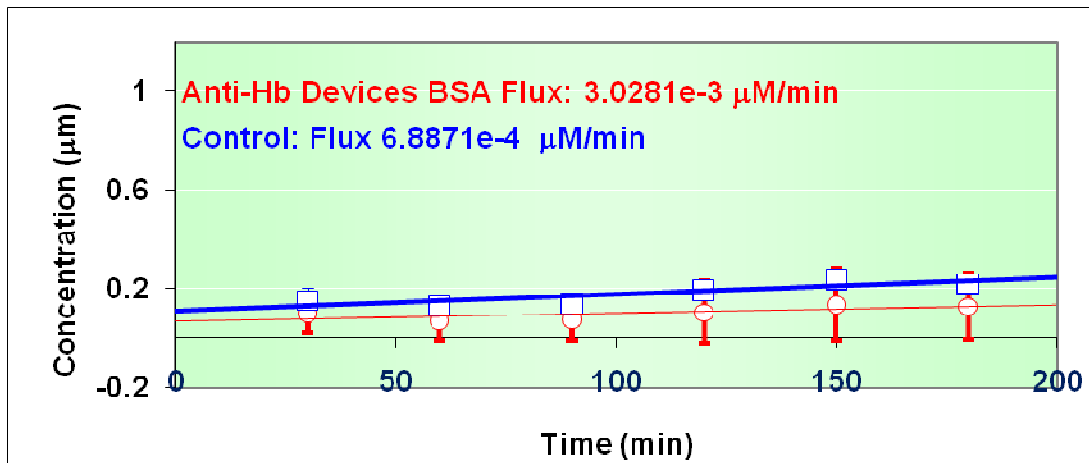


(b)

Figure  4.5.  Molecules transported through anti-Hb antibody functionalized membrane.  (a) Shows the comparison of Hb transport through anti-Hb antibody functionalized and non-functionalized native membrane. (b) Shows the comparison of BSA transport through anti-Hb antibody functionalized and non-functionalized native membrane. (n=4)

The increased flux of BSA was due to attractive potential generated by anti-BSA antibody. The phenomenon of 'facilitated transport' in presence of complementary antibody was verified by the functionalization of the nanochannels with anti-Hb antibodies. The flux of Hb in

27

functionalized membrane was significantly increased (17 times) as compared to the flux of Hb in control device. The flux of BSA was also increased (4 times) as compared to the flux of BSA in control device (Table 4.1, Figure 4.5(a)). Interestingly, the nanochannels were inherently selective for BSA before functionalization (separation factor $\beta$ is 0.33), but selectivity was switched towards Hb ($\beta$ is 1.5) after functionalization with anti-Hb antibodies. Therefore, protein selectivity of the membrane can be switched "on" for desired protein by surface modification of the nanochannels with antibodies specific for target protein.

### 4.4.3  Specific protein filtration in high protein background

Hemoglobin flux was recorded from mixture containing high concentration of BSA. The BSA concentration was increased to 20 µg/µl and 40 µg/µl keeping the Hb concentration at 1 µg/µl. Table 4.2 shows the separation factors of these devices.

Table 4.2. Permeation data and separation factor for control and functionalized membranes with increased concentration of BSA

| Device specification | | Transport rate of molecules (µm/min) | | Separation Factor | |
|---|---|---|---|---|---|
| | | BSA | Hb | $\gamma$ | $\beta$ |
| BSA : Hb = 20:1 | Control | 1.4931e-2 | 3.24e-4 | 46.08 | 0.02 |
| | Anti-Hb antibody | 1.968e-3 | 4.254e-3 | 0.46 | 2.16 |
| BSA : Hb = 40:1 | Control | 2.815e-2 | 2.46e-4 | 114.64 | 0.0087 |
| | Anti-Hb antibody | 1.421e-3 | 4.239e-3 | 0.335 | 2.98 |

The separation factor $\beta$ increased from 0.02 to 2.16 and from 0.009 to 2.98 for the cases when the BSA concentration was increased to twenty and forty times respectively (Table 4.2). However, the BSA which was flowing at a much faster pace in control devices due to its high concentration in feed mixture ceased to flow at higher flux through the functionalized

devices essentially decreasing γ from 46 to 0.02 and from 114 to 0.0087, respectively, again for

twenty and forty times increased BSA concentration (noise) in the feed solution.
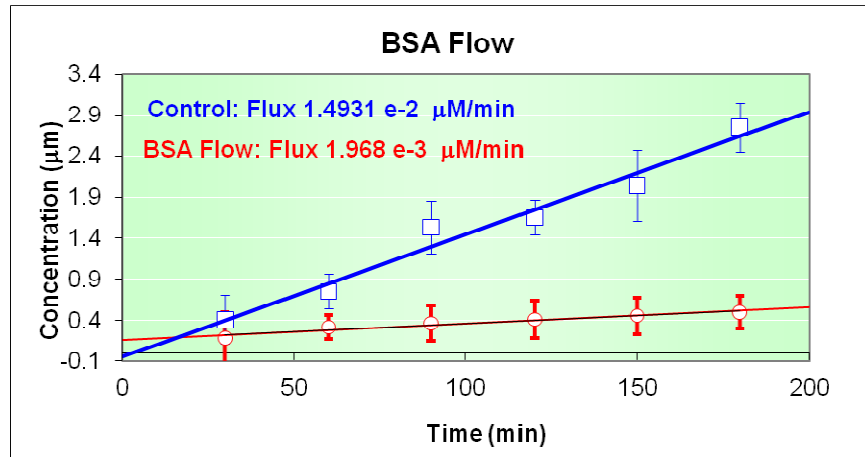


(a)
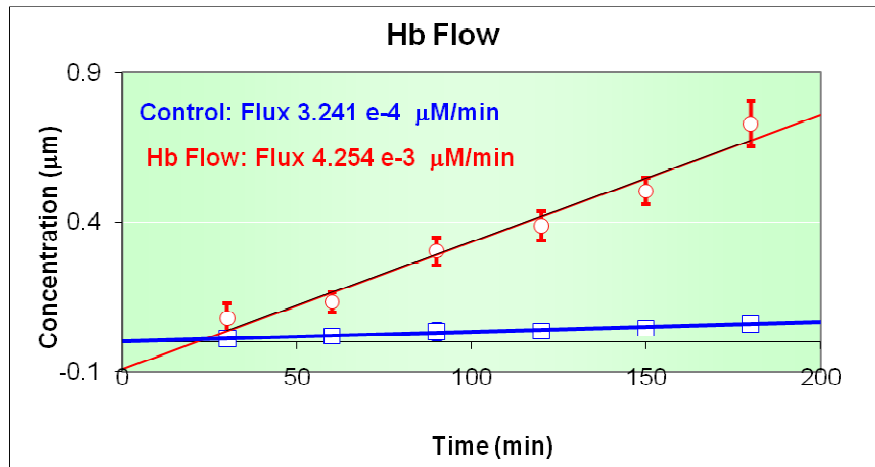


(b)

Figure 4.6.  Hb flow in control and anti-Hb antibody activated devices. Feed solution was BSA : Hb = 20:1.
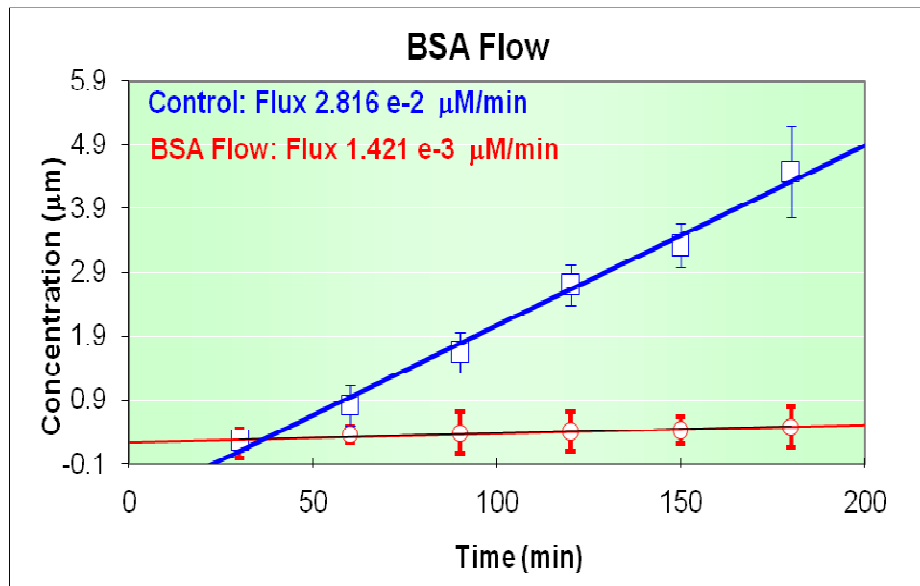
(a)
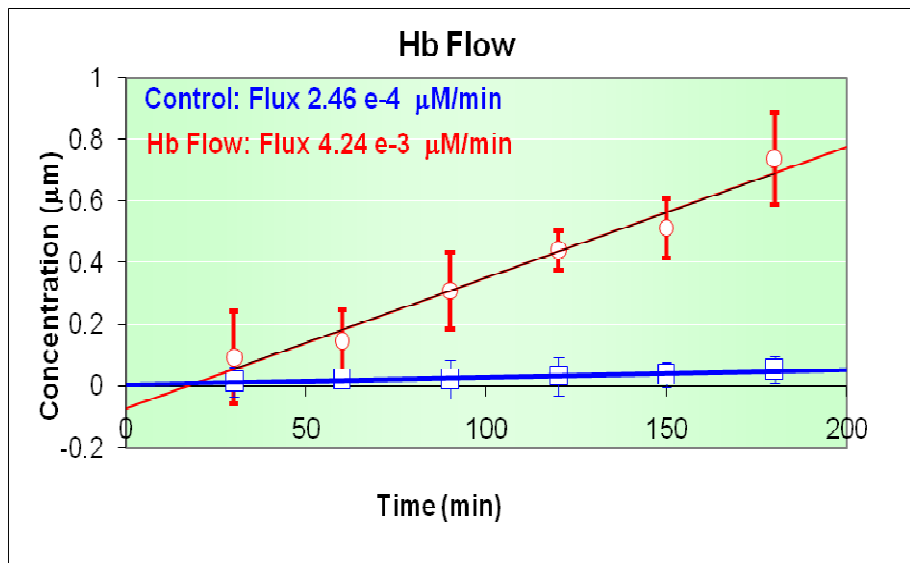


(b)

Figure 4.7.  Hb flow in control and anti-Hb antibody activated devices. Feed solution was BSA : Hb = 40:1.

Though there was increase in flux of BSA in both devices, the increase was insignificant as compared to increase in Hb flux. Figure 4.6 and Figure 4.7 shows the flux of molecules in these devices.

Table 4.3 reports the estimates of $\alpha_1$ and the corresponding p-values for varying comparisons of Protein 1 and Protein 2 with different types of device. From table 4.3, the concentration of the BSA was significantly higher than that of the Hb in the control sample. With anti-BSA Ab (anti-Hb Ab) devices, the concentrations of the BSA (Hb) increased than those in the control samples, especially for the concentration of BSA (Hb) with p-values less than .0001, which was consistent with facilitated transport theory. Furthermore, with the device of anti-BSA, the concentration of BSA was statistically higher than that of HB (p-value <0.0001). For anti Hb devices the p-value was 0.1388 (percentage expressed as 13.88%), meaning the p-value was not statistically significant at 95% confidence interval. This could be due to the favor of native membrane towards BSA in the control experiments. Statistically, Hb is 86.12% higher than BSA in anti-Hb devices. But the data with increased BSA concentration shows that indeed the flux of Hb increased significantly with immobilization of anti-Hb antibody with p value $\ll 0.5$.

Table 4.3. Statistical comparisons of Protein 1 and Protein 2

| Protein 1 | Protein 2 | Estimate of $\alpha_1$ (fixed effect of protein 1) | p-value |
|---|---|---|---|
| BSA in control device | Hb in control device | 0.14 | <.0001 |
| BSA in anti-BSA device | BSA in control device | 0.19 | <.0001 |
| Hb in anti-Hb device | Hb in control device | 0.26 | <.0001 |
| BSA in anti-BSA device | Hb in anti-BSA device | 0.19 | <.0001 |
| BSA in anti-Hb device | Hb in anti-Hb device | 0.06 | 0.1388 |

## 4.5  Discussion

The higher flux of BSA was observed in the control experiments. The carbonate groups on polycarbonate membrane have *pKa* of 2.5 and are negatively charged at pH 7.4. Both BSA

and Hb are negatively charged at pH 7.4 (pI: 4.6 for BSA and 6.8 for Hb) and experience electrostatic repulsion from negatively charged membrane surface and nanochannels. Ku and Stroeve demonstrated enhanced flux of molecules at their respective pIs and reported higher flux of BSA than Hb at their respective pIs.[5] This is because BSA is more hydrophilic than Hb and can align its axis along the nanochannel axis and diffuse with lesser hydrodynamic hindrance than Hb.[5]  We observed similar results: higher flux of BSA than Hb in polycarbonate membrane without any surface functionalization.

The increased flux of BSA through anti-BSA antibody functionalized membrane nanochannels is a case of facilitated transport. The diameter of nanochannels after functionalization is comparable to the size of BSA or Hb.  This can be considered as a cylindrical volume and thereby this small volume would constrain protein molecules to move through the nanochannel one after the other. The non-covalent binding forces between antigen and antibody exist over a very short distance of 1 Å.[78] It is proposed that presence of antibody (anti-BSA antibody in this case) on the inner walls of the nanochannel create attractive potential/field throughout the nanochannel and induces increased concentration of complementary BSA protein inside the nanochannels. Here each passing molecules has to interact with the antibodies attached on inner wall of the nanochannel. In the absence of anti-BSA antibody, BSA protein applied in feed solution will equilibrate on both sides of the membrane.  However, in the presence of antibody, the BSA specific antibody inside the nanochannel results in providing a pull to BSA proteins even at equilibrium overall increasing the total concentration of complementary protein inside the nanochannel, and subsequent passage of many more molecules across.

The association between anti-BSA antibody (Ab) and BSA protein (Ag) can be described by the equation,

$$Ag + Ab \underset{k_2}{\overset{k_1}{\rightleftharpoons}} Ag - Ab$$
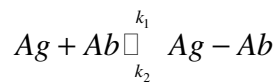
where $k_1$ and $k_2$ are the association and dissociation constants respectively. The Ag-Ab complex is dynamic in nature and exists in equilibrium between bound and free Ag molecules. According to the facilitated transport theory, the diffusion coefficient for the species that binds to the functionalized nanochannels is smaller than the diffusion coefficient for the species that does not. The formation of the Ab-Ag complex should "hold up" the molecule, effectively lowering its diffusivity. The flux of a non-interacting particle is given by $J = (n/\tau)(c_1 - c_2)$, where $\tau$ is the regular Mean First Passage Time (MFPT) for the interacting particle to cross the channel, $n$ is the measure of the particle number, $c_1$ is the concentration of the bath on one side of the channel and $c_2$ is the concentration on the other side.[72, 79] The lowered diffusivity (that results in longer $\tau$) however is over-compensated from the attractive potential stemming from the surface-bound Ab. Such attractive potential causes an increase of the concentration of the respective Ag in the channel, $n$, way more than the increase in $\tau$. It has been shown earlier that the flux is enhanced when the channel has an attractive potential, as compared to no potential and the flux is reduced when the channel has a repulsive potential, as compared to no potential.[72] Thus, the drop in diffusivity is compensated by the interaction-based concentration enhancement and in the net, flux is higher when there is an attractive interaction. It is important to note here that the diffusivity $D$ cannot be considered a constant; rather the dependence of diffusion on the potential itself is built into an exponential dependence of the $\tau$ with potential. Even if such dependence is specifically included, we get $D = D_o e^{-|\phi|}$ where $D_o$ is diffusion coefficient at zero penetrate concentration and $\phi$ is the potential arising from molecular interactions.[80] Our results clearly show that interactions of surface bound antibodies alter the diffusive flow of specific proteins. Facilitated transport theory based findings have highlighted the effects of such molecule-nanochannel interactions where binding events can overcome the Debye length effects.[72].

**4.6 Conclusion**

It was shown that the functionalized polycarbonate membrane containing nanochannels can selectively filter a specific protein. The importance of this technique lies in the fact that at the onset of disease, the disease related biomarkers (target molecule, nanogram/ml) are hard to be detected in the pool of thousands of other species in biospecimens (biological noise, milligram/ml). This approach can filter these biomarkers on the basis of their biological interaction, not on their physicochemical properties or size. This technique can have wide applications in molecular recognition studies, pharmacology, purification of specific biomolecules, and early disease diagnosis as a result of specific protein isolation and detection from whole biospecimens. This technique, for using membranes to concentrate and condense low-abundant biomarkers, is the first biomimetic demonstration of facilitated transport phenomena that occurs in biological pathways. The nanochannel size and the porosity can be tweaked to define the number of nanochannels and how much interaction in each nanochannel can occur. Synthetic nanochannels are robust versatile platforms with the possibility of integrating electronic, optical and chemical probes to enhance the signal sensitivity. The low-cost and rapid fabrication of functionalized nano-membranes can be a major enabling factor towards designing serial or parallel functionalized membranes that can each identify and concentrate different biomarkers. Such an integrated design can not only provide clear and reliable identification of various biomarkers but can also be used to distinguish patients who respond to treatment and therapy.

CHAPTER 5

EFFECT OF FLUORESCENCE ON PROTEIN INTERACTION IN NANOCHANNELS


Optical imaging using organic dyes and quantum dots are very attractive as they can provide in-situ information about the interactions and reactions happening in a system. While the advancement in nanotechnology pushes the limits to devices operating at nanoscale, there is unknown phenomenon existing at that length scale. This chapter is essentially the extension of chapter four, here; effect of fluorescence dye tagged protein was used as protein mixture to filter through antibody immobilized devices.


**5.1 Device fabrication**

Polycarbonate membranes with different diameter nanochannels were activated using UV/Ozone plasma for 220 seconds with shiny side facing up. For PDMS casting, Sylgard 184 was mixed in 10:1 ratio and polymerized at 110 ˚C for 4 hours. The holes of 6 mm diameter were made using biopsy punch. Two layers of PDMS were aligned and membrane was sealed in between using Sylgard 184 in ratio 20:1 and left overnight at room temperature. The membranes were 6 µm thick with nanochannel density of $6X10^8$ channels/cm$^2$. The effective filtration area was 110 mm$^2$.

Carboxyl groups were generated using oxygen plasma. Rabbit IgG antibody was diluted 1:500 in PBS with 20 mM 1-ethyl-3-(3-dimethylaminopropyl) carbodiimide (EDC) and 10 mM *N*-Hydroxysuccinimide (NHS) (Sigma, Saint Louis). The antibody solution was applied on the upper side of the device (UV activated surface) and incubated at 4 $^o$C for overnight. The devices were then washed with copious amount of PBS, and incubated with 4% goat serum in PBS for

one hour to block unreacted carboxyl groups and decrease the non-specific protein adsorption. It was then washed vigorously and used for filtration.

## 5.2  Filtration of fluorescent antibodies

To investigate if decrease in pore size has any effect on molecule transportation, different pore size membranes with pore diameters of 200, 100, 50 and 15 nm. The membranes were functionalized with rabbit IgG and used to separate mixture of two secondary antibodies, goat anti-rabbit IgG tagged with Alexa 488 and Goat anti mouse IgG1 tagged with Alexa 546. The antibody concentration in reservoir solution was measured as a function of the fluorescence of respective tagged dyes.

Another experiment was conducted to see if presence of fluorescent molecule had any effect on molecule mobility through nanochannels. Here, the fluorescent tags of antibodies in sample mixture were exchanged. The mixture was then filtered again through 15 nm membranes immobilized with rabbit IgG antibodies.

## 5.3 Results

Flux of secondary antibodies was measured across different diameter nanochannels. For 200 and 100 nm pore size (Figure 5.1 (a&b)), the flux of goat anti-mouse IgG1 (non-complementary) was much higher than goat anti-rabbit IgG (complementary). These devices behaved like affinity chromatography column. Such columns hold the complementary protein and available space is open for movement of free non-interacting proteins. However, when the membrane pores size was decreased to 50 nm (Figure 5.1(c)); there was a transition in flux. The flux of complementary antibody, i.e. anti-rabbit IgG increased than that for non-complementary antibody.  For 15 nm (Figure 5.1(d)), the flux of complementary antibody tagged with Alexa 488 was higher than non-complementary which is reverse of what we observed in 200 and 100 nm diameter pore membranes.

36
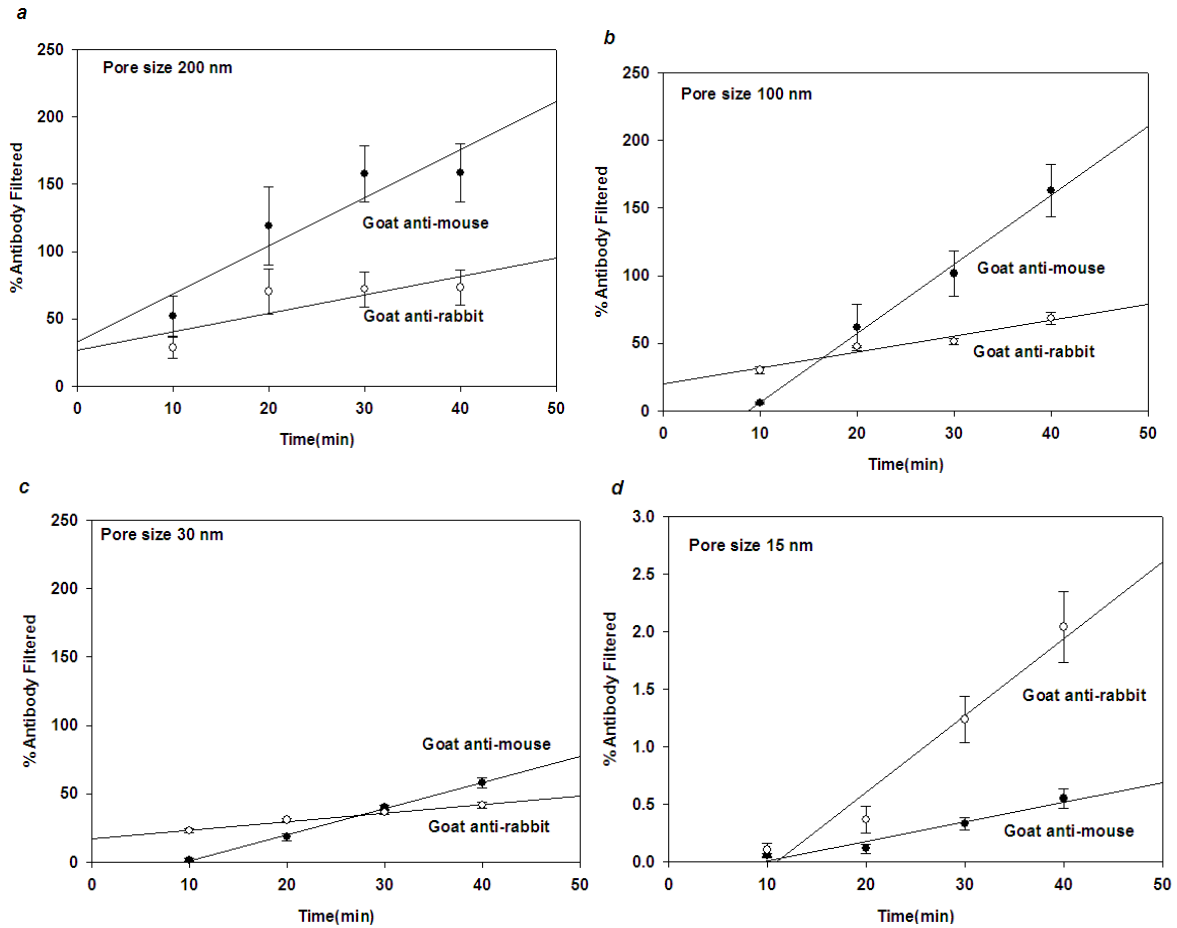
Figure 5.1. Filtration of antibodies through different diameter nanochannels. (a) For 200 nm, flux of goat anti-mouse antibody is higher; (b) for 100 nm, flux of goat anit-mouse antibody increases after some time; (c) for 50 nm membranes, flux of goat anit-mouse antibody increase after 30 min; (d) flux of goat anti-rabbit antibody is higher.

The attractive potential created by surface antibody is too high and there is no free space for non-interacting proteins to pass through. We hypothesize that if the membrane behaved selectively permeating transport of only interacting molecules, then interchanging the fluorescence tags on sample antibodies should reverse the fluorescent signal, without changing the filtration specificity. However, interchanging the dye on two antibodies in feed solution didn't alter the membrane selectivity for filtering the molecule tagged with Alexa 488. The protein tagged with Alexa 488 always had higher flux than others.

**5.4 Discussion**

Surface properties and presence of fluorescent dyes in feed solution has dominant affect on liquid flowing through nanochannels. Both Alexa 488 and Alexa 546 are negatively charged molecules, however, Alexa 546 has 6 methyl whereas Alexa 488 has 2 amine groups side chain, that makes Alexa 546 much more hydrophobic than alexa 488.[81] The molecules tagged with Alexa 546 would thus be repelled from the hydrophilic surfaces. For this reason, the molecule tagged with Alexa 488 always predominantly passed through the channels. Further, antigen-antibody interaction is not fully understood in nano-confinements.

CHAPTER 6

SELF-ASSEMBLED PDMS MICROPORES- HYDROPHILLIC INTERFACING FOR THERMAL

MICRO ASSEMBLY PATTERNING (HITMAP)


**6.1 Introduction**

Polydimethylsiloxane (PDMS) is optically clear organosilane polymer commonly used to fabricate microfluidic channels using soft lithography. It can sustain high temperatures, as compared to other polymers. It has biologically relevant Young's Modulus and is biologically inert.[18] Various methods have been demonstrated to fabricate microfluidic devices with varying channel sizes and multilevel channel structures [23-30]. Inexpensive methods using nylon fiber and low surface energy templates have also been recently reported[32, 33]. Removal of nylon templates requires organic solvents that cause the PDMS to swell and low energy templates are limited in dimensions. Simple porous membranes with pore sizes of 4-6 μm has been reported using water as porogen, and used as pH sensors[34]. Commercially, track etched membranes are made by bombardment of heavy ions on polymer surface such as polycarbonate and polyethylene terephthalate[82]. Soft lithography has provided many powerful techniques to fabricate channels, where a master is first fabricated using photolithography and the elastomeric stamp is then made with patterned relief structures.

PDMS has been a material of choice for electrical wire insulations for decades owing to its hydrophobic nature that is easily regained due to diffusion of low molar mass PDMS to the surfaces[83]. During polymerization the macromolecules are connected into polymeric networks that are three-dimensional. The cross linking reaction results into increasing molecular weight and reaches *gel point* where macromolecular network extends to the whole

39

sample and coexists with the loose branched networks that are not yet become a part of the network. The network continues to grow until all remaining molecules are used up as part of the one big network. The reactions at gel point (GP) have important implications that result into increased stiffness and infinite viscosity[84]. At GP, phase transition of the pre-polymer into a rubber-like material occurs. The process has an associated decrease in the entropy of the system, which essentially results from the reduced number of configurations that molecular sub-units can have after polymerization.[85, 86] The configurations that the subunits can take and the probability for these subunits to become part of a large network are independent, thus the overall change in the free energy can be separated into enthalpic and entropic terms. The entropy penalty should result into enthalpy gain if, like in the case of silicates, PDMS immersed particles don't get intercalated during polymerization[87]. The work presented gains its strength from the interactions of hydrophilic-hydrophobic interactions at the interface of PDMS and nano-/micro-materials (beads, particles, droplets). The reduction in free energy results into useful enthalpy that pushes immiscible entities out of the resulting semi-solid polymer. This is first demonstration of harnessing this enthalpy to get useful work done in a quick, low-cost, bench-top technique for porous membrane fabrication, using inherent hydrophobic property of PDMS.

We presented simple approaches using bench-top tools to fabricate aligned microchannels and porous membranes in PDMS within an hour. These methods used materials like nanoparticles, magnets, polyurethane beads and acetone, and implemented with minimal need of special facilities or equipment. The formation of channels was based on the repulsion of hydrophobic polymer for hydrophilic molecules/materials that lead to phase separation and channel formation during polymerization. The hydrophilic particles in PDMS clutter together, in both solid and liquid phases, essentially more like a reverse phenomenon of micelle formation in hydrophilic environments.

Figure 6.1 shows the motivation and simple demonstration of the underlying mechanism, where blue ink was homogenously mixed in the liquid precursor of PDMS. As soon

as the solution was exposed to heat from bottom, the polymerization ensued from the bottom of the well. First almost all ink droplets clumped together as a big ball and then the ball started rising away from the bottom (hot side) in the direction of polymerization.



|     |     |     |     |
| :-: | :-: | :-: | :-: |
| (a) | (b) | (c) | (d) |
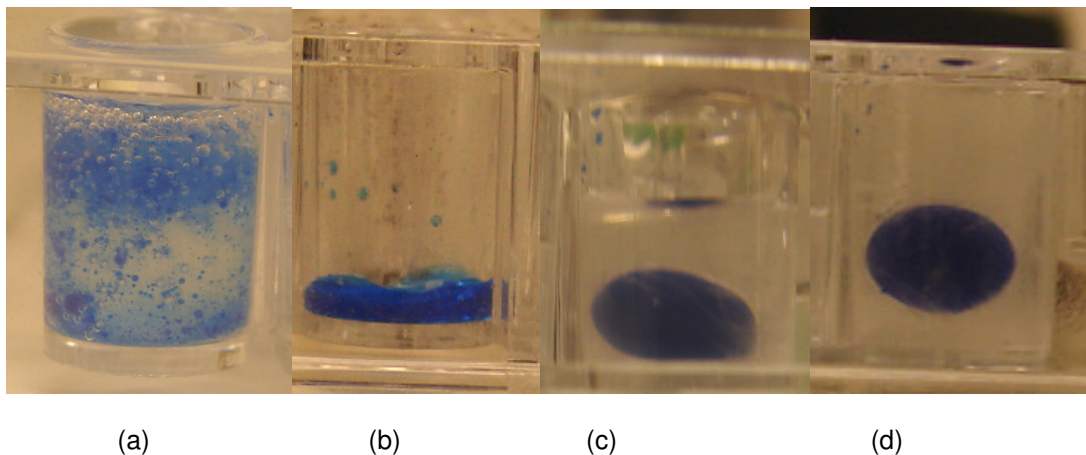
Figure 6.1. Images showing behavior of blue ink as the PDMS polymerizes (a) Blue ink is homogenously mixed in PDMS pre-cursor (b) Ink gradually forms a cluster as low molar mass PDMS networks are formed (c) As the networks of PDMS become larger, the ink balls becomes spherical (d) the ball of ink rises as PDMS networks becomes large enough to cover whole area of the chamber.

We used this phenomenon to design techniques for simple bench-top porous PDMS membrane formation. The techniques are called Hydrophilic Interfacing for Thermal Micro Assembly Patterning (HITMAP). Such PDMS membranes can be manufactured for use in pervaporation experiments to remove organics, as soft elastic substrates to study cell movement, for cell adhesion studies, hydrogen storage and for aligned microfluidics[20, 21, 88]. The basic mechanism is believed to be the same for all the materials that have been used and reported here.

## 6.2 Experimental Methods

Polyurethane beads, iron nanoparticles, sylgard 184 and acetone were used as received. Ultrapure grade water with a conductivity of 18.2 MΩ cm was used in all experiments.

41

### 6.2.1 Polyurethane Beads

Polyurethane beads are hydrophilic and thus were used to fabricate aligned channels. The Lubrizol polyurethane beads were kept on a clean glass petridish and heated at 100 ºC for 2 minutes.  The PDMS was mixed in a ratio of 10:1 (oligomer:curing agent) and poured into the dish on top of the beads.  Temperature variation studies were done to tune the optimum temperature for the formation of channels.

### 6.2.2 Iron Particles

For precise channel formation, 30 nm iron particles were employed. The particles were kept on a petri dish and PDMS was poured on top of these nanoparticles.  PDMS was polymerized on hotplate while a magnet was use to align iron particles as the particles moved upwards.  The magnet was not used to cause the movement but just to give directionality and align the channels.

### 6.2.3  Acetone in PDMS

Acetone was also used to make thin PDMS membranes of 1 mm thickness.  Acetone is a known solvent/swelling agent of PDMS[89].  The acetone was mixed with PDMS in the ratio of 0.5:2, degassed and a thin layer of mixture was made over the glass plate. The polymer was cured at 80 ºC.

### 6.2.4  Condensed Vapors

In this approach, the condensed water in PDMS was used to create hollow 1-D channels. PDMS was mixed in the ratio of 10:1 (oligomer:curing agent), degassed and kept at -18 ºC overnight.  It was then degassed again at room temperature before polymerization.  The polymer was then polymerized over the hot plate at different temperatures.

**6.3 Results**

The formation of channels was examined microscopically. For test the channel continuity, the movement of ions was studied across the channels.

*6.3.1 Polyurethane Bead Channels*

These beads formed channels in the range of hundreds of micrometers. Figure 6.2 shows the confocal micrographs of 517 μm diameter channels. These structures were vertically aligned but closed from one end (bottom). The formation was not uniform throughout the channel and slight constriction was observed at the bottom. These membranes were cut open from the bottom to obtain through channels. An important requirement to form these channels was the hydrophilicity of bead surfaces. Interestingly, there was a range of temperature from 113 ºC to 120 ºC within which the channel formation occurred. Below and above this temperature, the beads/vapors were predominantly entrapped inside the polymer. It is important to note here that track-etched membranes with conical pores have found many applications for biophysical studies[90]. The pore with varying inner diameters can be defined in terms of the narrowest diameter as that would be important for similar applications as that of conical pores.
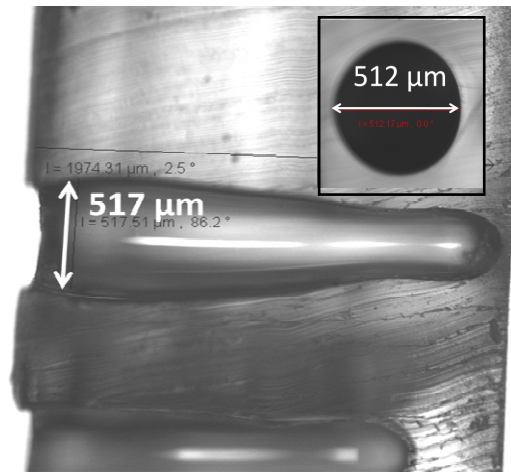


Figure 6.2. Channels made with polyurethane beads. The inset shows the top view of channel.

*6.3.2 Iron Particles*

In the presence of magnetic field, the magnetic particles typically produce one-dimensional (1-D) chains with their magnetic dipoles aligned head-to-tail, parallel to magnetic field[91, 92]. A strong magnet was used (left inset to Figure 6.3) to give directionality to the movement of iron nanoparticles. The particles made 1-D linear pores in the PDMS (Figure 6.3). The right inset in Figure 6.3 shows magnified image showing particles joined together forming a linear chain. Vertical channels still formed even in the absence of magnetic field. The pore diameters ranged between 4-7 μm. The Confocal micrographs of one channel are shown in Figure 6.4.
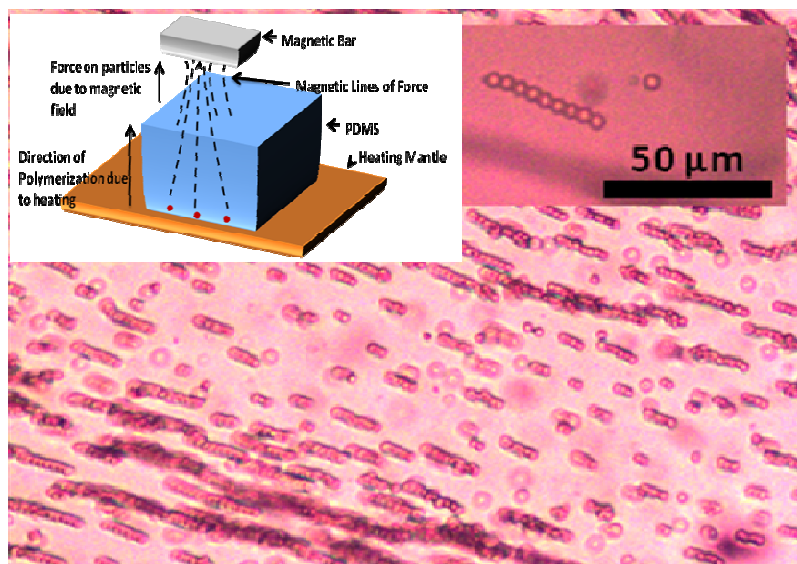


Figure 6.3. Movement of iron particles in the magnetic field**.** Optical images showing the movement of iron particles and self-alignment as linear chain under magnetic field. Left inset shows schematic of the process. Right inset shows a magnified view of one chain.

*6.3.3 Acetone for Membrane*

Acetone is a volatile solvent and evaporates at room temperature. Heating acetone mixed in PDMS removed acetone from the PDMS mixture leaving behind transparent ~1 mm thick PDMS membrane with pores of diameters ranging between 10-20 μm (Figure 6.5). The porosity and pore size was seen to be inversely related with polymerization temperature.
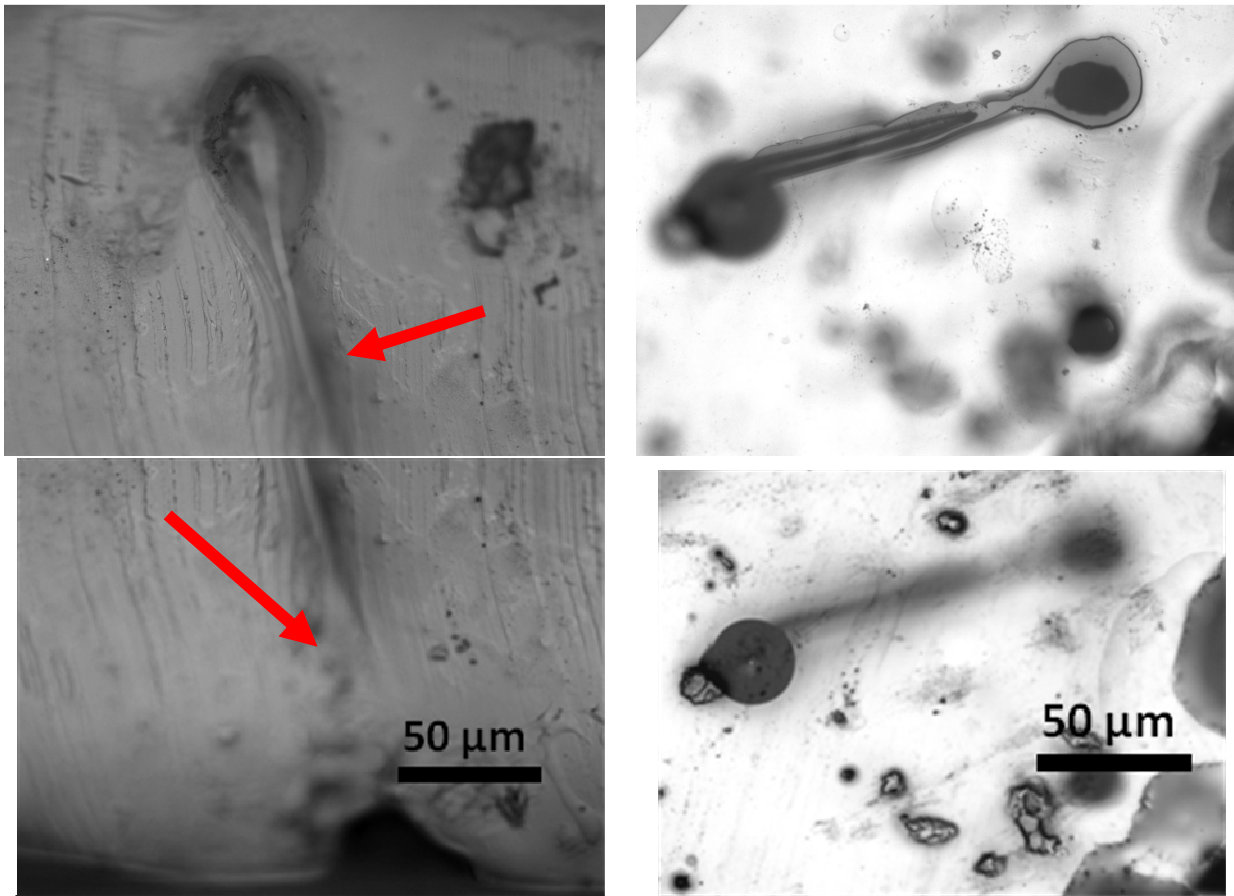
(a)                                                    (b)

Figure 6.4. Microchannels from iron particles. Confocal micrographs of channels formed by iron particles. (a) A 10 µm diameter channel was formed. Arrows show start and end of the particle journey. (b) Images at different focal planes show the formation of channels inside the PDMS.
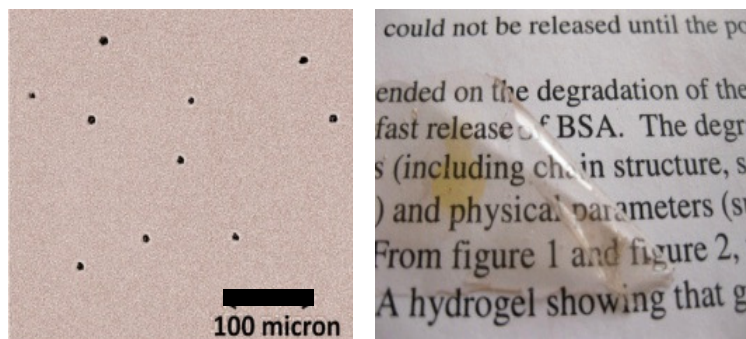


(a)                                                    (b)

Figure 6.5. PDMS membrane made using acetone. (a) Optical image with bar scale of 100 micron. (b) Optical image showing the transparent membrane.

*6.3.4 Condensed Vapors*

      The directional removal of entrapped water vapors also resulted in micro-channel formation. Removal of water and associated channel formation was observed to depend on two factors; polymerization temperature and percentage of curing agent in mixture. As shown in Figures 6.6, the pore diameters decreased gradually with the increase in polymerization temperature from 90 ℃ to 110 ℃. Above 110 ℃ almost a plateau was reached. An order more number of channels were formed at higher temperature.



(a)



(b)
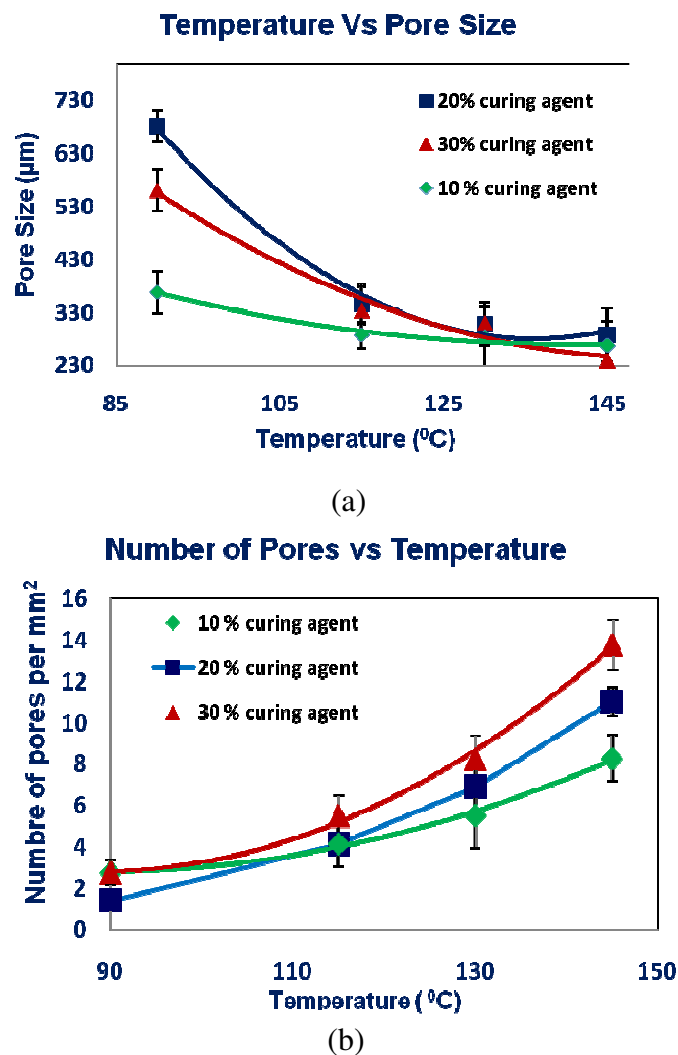
Figure 6.6. Plot (a) Variation in pore diamaters and (b) porosity with polymerization temperature for different ratio of curing agent in PDMS.

46

(a)                                                    (b)



(c)                                                    (d)
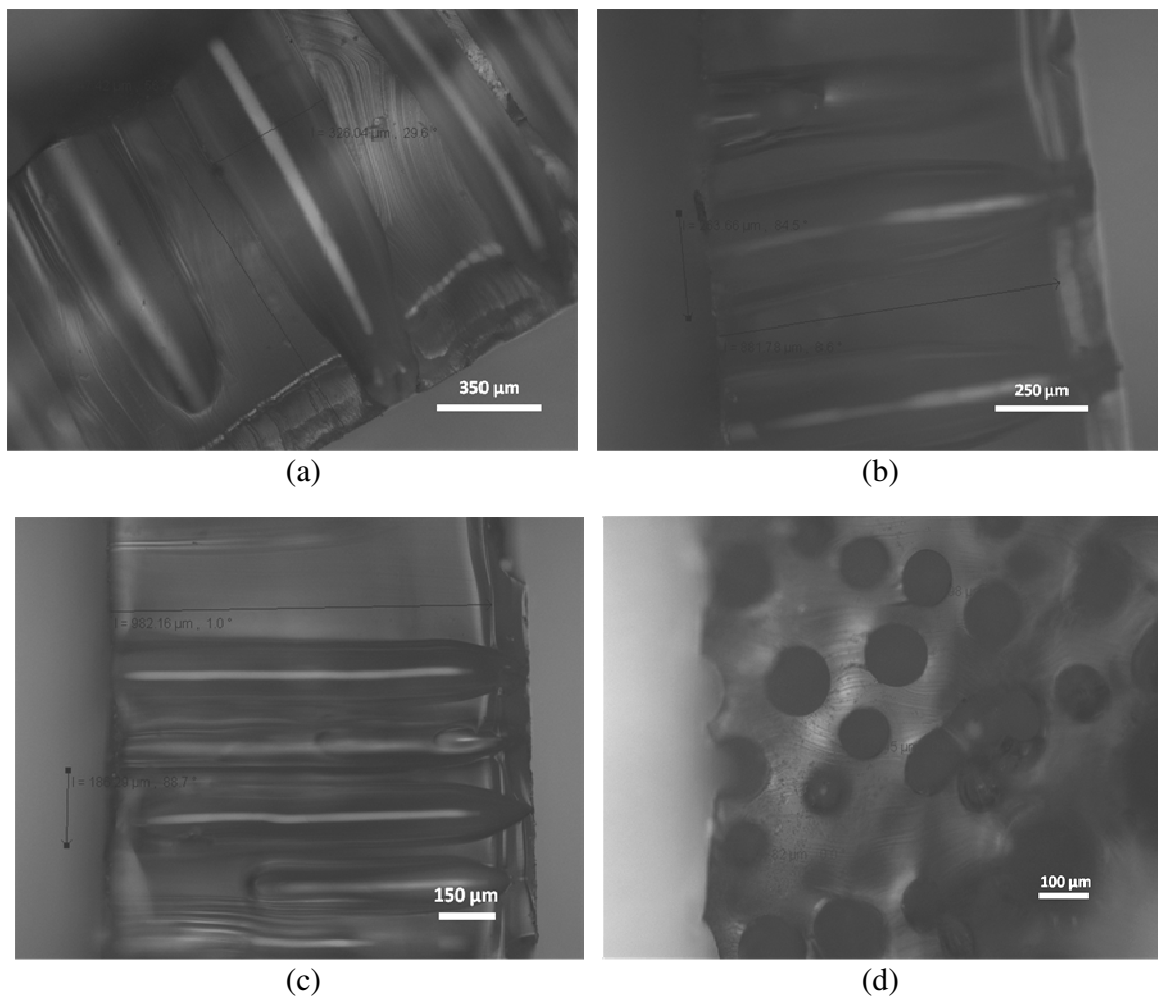
Figure 6.7.  Uniformity of channels

Lateral sections of channels made by condensed vapors inside PDMS for (a) 10%, (b) 20%, and (c) 30% curing agent in PDMS. The channel diameters decreased with increase in the concentration of the curing agent in PDMS.  (d) Top view of the channels formed with 30% curing agent in PDMS.

The number of pores and porosity varied with the curing temperature at three concentrations of

PDMS curing agent.  Figure 6.7 shows the uniformity of the channels formed at different volume

percetages of curing agent with respect to various temepratures.

*6.3.5 Current-Voltage Measurement*

　　　The membranes are tested for their continuity and permeability using ionic conductivity measurements.　The system for measurements was same as is used for the measurement through single pore[93].　An *N* number of channels with same diameter and length can be considered to have same resistance and conductivity, if we approximate the effects of surface changes from each channel wall to be equal (Figure 6.8(a)).



6 $\acute{R}$ in parallel

$R = \acute{R}/6$

$$R = \frac{1}{\left(\frac{1}{\acute{R}}+\frac{1}{\acute{R}}+\frac{1}{\acute{R}}+\frac{1}{\acute{R}}+\frac{1}{\acute{R}}+\frac{1}{\acute{R}}\right)} = \frac{\acute{R}}{6}$$
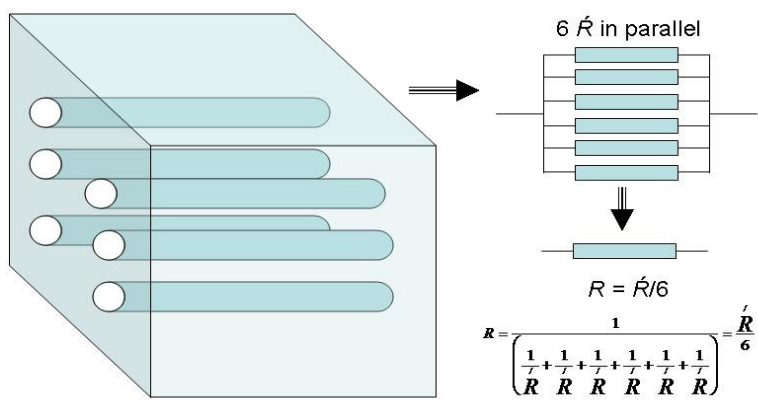
(a)
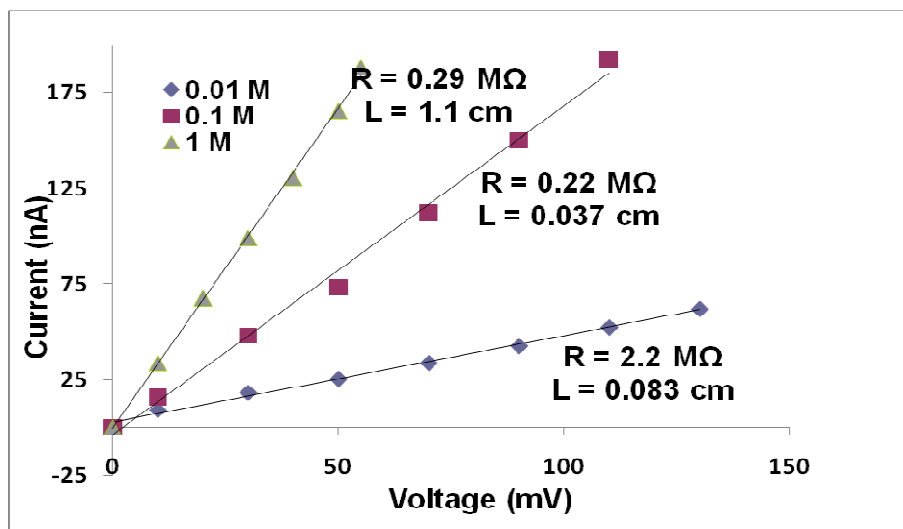


(b)

Figure 6.8.　(a) Circuit equivalent to membrane. (b) *I-V* data from membrane at different molarities.　Resistance (measured from slope) and calculated length is shown with each curve.

The equivalent resistance $R$ of a network of $N$ parallel and equal resistances $\acute{R}$ is thus $\acute{R}/N$. The current-voltage (*I-V*) data was measured with a patch-clamp measurement system developed in-house. The voltage bias was applied across the membranes and conductivity of KCl solution was measured across directionally aligned channels. A membrane with 6 pores having diameter of 300±10 μm was used. This membrane was made using polyurethane beads. The channels were closed from the bottom and were sliced open to make through channels. The *I-V* data across the membranes was measured at different concentrations of KCl solution and conductivity was calculated for different molarities using $\sigma = nq\mu$ where $\sigma$ is the conductivity of the channels (which is inverse of resistivity $\rho$), $n$ was the number of ions, $q$ was the unit charge and $\mu$ is the mobility ions. The ionic mobility values were used as reported before[94]. The resistance $R$ was calculated from the inverse of slope from *I-V* plots for each molarity (Figure 6.8(b)). The membrane can be modeled as a network of 6 resistors in parallel (*N*=6) and the measured $R$ is the equivalent resistance of the 6 pore membrane that was test for electrical continuity and permeability using ionic conductivity.
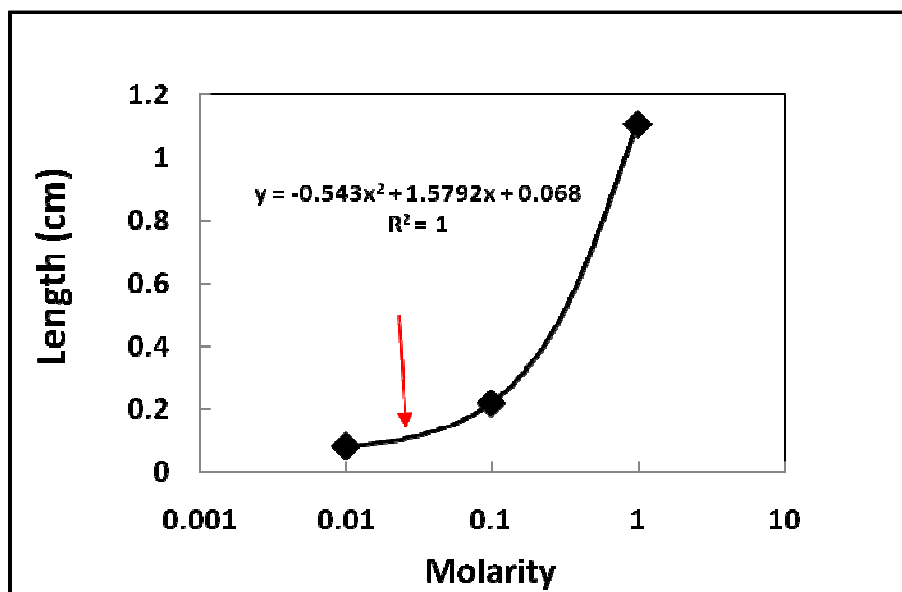


Figure 6.9. Relation between calculated length of channel and molarity of KCl used.

The length of channel was calculated using, $R = \rho L / A$, where $A$ was measured from images of the membrane (0.2826 cm$^2$) and $R$ was the inverse of the slopes of the curves in Figure 6.8(b). The value of $R$ was divided by 6 to calculate $L$ of individual pore. A linear relation was observed between calculated length and the molarity of KCl solution (Figure 6.9). The calculated length of channel is very large especially for lower molarity indicating enormous charge build up and silanol dissociation on PDMS walls decreasing the conductivity of ions.

## 6.4 Discussion

For polyurethane Beads, the curing temperature of PDMS was above the melting temperature of polyurethane beads, so the beads melted and formed thick viscous nucleations. The change in entropy and enthalpy at GP and diffusion of low molar mass hydrophobic PDMS chains slowly 'kicked' the molten beads out while the PDMS polymerized. This movement resulted in the trails/tracks in the form of empty channels in the PDMS bulk. Therefore, for this kind of channel formation surface characteristics of particles and their chemical interaction with polymer is critical.

For iron Particles, it was observed that the force exerted by hydrophobic PDMS was not enough to push all the particles upward/out of PDMS. The rate of polymerization at the particle-polymer interface was very fast as metal particles would get hot and result in localized polymerization of the PDMS in their vicinity. This resulted in the capture of the particles inside rather than pushing them out. An external upward force in the form of controlled magnetic or conductive field served two purposes: (1). Moved all particles against the downward gravitational force and localized polymerization, and (2) Aligned the particles. The expected outcome was the formation of 30 nm diameter channels, but the viscosity of liquid PDMS collapsed the chains forming small bundles of particles in the range of micrometers. The outward movement of the bundled particles along with polymerization from the bottom formed

50

channels of dimensions ranging between 4-7 µm diameters. An important point here is the versatility. Jackman et al. have demonstrated 5 µm aligned pores using soft lithography (with a photolithographically defined master)[95]. The approach presented here does not provide the level of alignment that can be achieved with soft lithography, but it essentially provides channels in the same range using no lithography and with just a hotplate and nanoparticles. The whole process can be completed within 30 minutes from start to end. The precision in alignment versus cost and time are essential trade-offs here. For better alignment of the microchannels in the presented approach, charged nanoparticles can be accurately positioned on a charged substrate utilizing the self-limiting interactions[96-98]. Single iron nanoparticles or microparticles can be placed precisely at particular locations before polymerization using such interactions; many configurations of this approach can be employed to produce 1-D guided channels *in any* pattern, without using lithography or contact processes.

For acetone based membranes, polymerized as well as nascent PDMS swells in the presence of certain organic solvents like ethanol. These solvents are volatile at room temperature, their removal from surface at high temperature leaves behind the channels while the surrounding polymers solidify. Due to volatility, there may be a limitation on the thickness of membranes formed using this technique.

For condensed vapor droplets, as the temperature increased, smaller diameter channels were obtained. This can be explained in terms of the speed with which scattered droplets clumped together while moving up in the polymer. At lower temperatures (around 90 ℃), the motion of hydrophillic droplets increases slowly with increase in temperature from 0-90 ℃. The hydrophillic vapors tend to combine together, growing to micrometer size, while moving and forming channels. On the other hand, at higher temperatures (~120 ℃), the upward movement was faster; the vapors could not grow and cluster, so formed smaller diameter channels. Increase in pore density was also a result of many more un-clustered smaller

51

droplets coming up at higher temperature than those at lower temperatures. It was thus expected and indeed observed.

The electrophoretic mobility and zeta potential of the PDMS membrane decreases with increase in ionic strength/molarity of solution[99], which reduces the contribution of surface charges towards resistance of PDMS. The overall resistance decreased with increase in molarity for two reasons: (i) Reduction in surface charge contribution; (ii) Increase ionic mobility and number of charge carriers. The length of pores calculations included $\rho$ (resistivity) which is inverse of conductivity $\sigma$, calculated from $\sigma = 1/\rho = n_{KCl}q(\mu_K + \mu_{Cl})$, where $n_{KCl}$ was the number of ions of KCl, $q$ was electronic charge and $\mu_K$, $\mu_{Cl}$ were the mobilities of potassium and chloride ions[94]. For constant $A$, $L$ is proportional to $(R/\rho)$.

As the molarity decreased by an order, resistivity increased by an order. However, increase in $R$ was more than an order, which overall increased the calculated length of channels. This increase in resistance is contributed by the dominant surface charges at low molarity and dissociation of silanol groups.

We propose that there is direct relation between molarity and resistance developed due to presence of surface charges on PDMS channels, called $R_{PDMS}$ (i.e. $Molarity \propto 1/R_{PDMS}$). For constant $A$, $L_{pore} = (R_{channel} + R_{PDMS})/\rho$, where $R_{channel}$ is resistance due to channel and $R_{PDMS}$ is resistance developed due to charges on the pore surfaces. As the molarity decreased by an order, $R_{PDMS}$ increased by an order, which resulted in increase in the calculated length of the channel by an order (due to contribution of charges).

**6.5 Conclusion**

This work demonstrated the use of bench-top techniques to fabricate PDMS channels and membranes. Several parameters like polymerization temperature, nano/microparticle

properties, magnetic strength and solvent concentration characterize the physical dimensions of the end characteristics and dimensions of the channels. Based on the evidence of channel formation through hydrophillic beads, particles and vapors, many more material can be used for rapid formation of polymer membranes in particular patterns.

Owing to the excellent biological, physical, chemical and mechanical properties of PDMS, these membranes can be used for biological filtration of cells, proteins and as dialyzer membranes. There is possibility of making cylindrical or spherical membrane, very useful for *in vivo* studies, e.g. for making synthetic alveoli in lungs or drug delivery particles. Perforated membrane coatings on biomedical implants can offer better tissue growth with increased surface area. Fabrication of single micropore can be used to study cell movement across the PDMS membrane for biomechanical studies.

CHAPTER 7

FUTURE WORK

The goal of nanobiotechnology based devices is to interrogate interfaces or biomolecules sensing at the same scale as of the analyte of interest. These surfaces offer newer undiscovered properties for application in all fields. As described in this thesis, first the novel method to design DNA probe and ss-DNA selectivity for lung cancer mutation can be extended to any point mutation for various diseases. Similarly active filtration of molecules through nanochannels can be used to purify several biomarker proteins. The technique can itself be extended to detect proteins or DNA molecules. Solid state thin nanopores can be used to increase flux across the channels as they provide robust control over the size. Single pore can be manufactured and they can with stand wide range of analyte solutions and buffers.

**7.1 Detection of point mutation in ss-DNA**

Point mutation is the root causes of many diseases such as cystic fibrosis, sickle cell anemia and most of the cancers. The electrical detection of ss-DNA can be used for either of disease for high assay sensitivity. In thesis, Agilent probe station was used to measure small change in current that restrict the present design to be extended as POC (point-of-care) device. There are automated devices in market that can be integrated with present design and measure electrical changes, however, still the technique will be restricted to specialized laboratories.

**7.2 Electrical solid-state sensor to detect biologically relevant markers**

As an extension of active filter device, solid state nanopores can be used to purify proteins. Solid state technology provides control over pore size, thickness and porosity.

Decreased length of channel will enhance flux across the pore. In single solid state nanopore, the electrical detection of ss-DNA was previously reported. Integration of solid state technology and filtration of proteins discussed in thesis can be used to electrically detect the movement of single protein across the channel (Figure 7.1). A dip in current is expected as molecule passes the pore, blocking the current stemmed from electrolyte. Such a device is expected to have very high sensitivity. Further, for enhanced selectivity aptamers can be employed instead of antibodies. A step ahead, pores can be tuned to bigger size of around 10 micrometer and cells can be selectively filtered. Such a device if capable to detect single CTC (circulating tumor cell) will have huge impact on cancer studies.
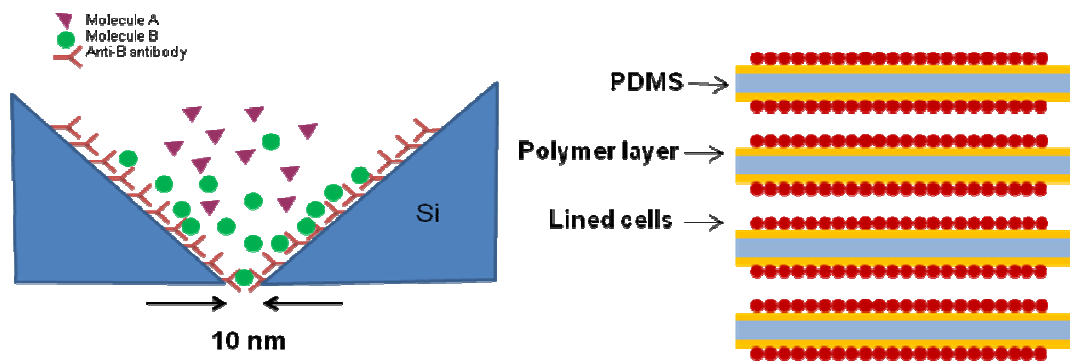


Figure 7.1. (a) Device for electrical detection of proteins (b) Top view of microchannel lined with cells

## 7.3 Coating of biological compatible composite on self aligned microchannels for cell filtration

PDMS channels can be coated with biocompatible film. Cells can be grown on walls of PDMS (Figure 7.1 (b)). Such an integration of device can have impact on cell directed growth of neurons. May be this kind of device can be used to study *in vitro*, the type of cell that promote growth of neurons or migration of cancer across corpus callosum .

REFERENCES

1.    Edwards, R., *Immunoassays: essential data.* 1996: John Wiley & Sons Inc.
2.    Jirage, K.B., J.C. Hulteen, and C.R. Martin, *Nanotubule-based molecular-filtration membranes.* Science, 1997. **278**(5338): p. 655.
3.    Savariar, E.N., K. Krishnamoorthy, and S. Thayumanavan, *Molecular discrimination inside polymer nanotubules.* Nature Nanotechnology, 2008. **3**(2): p. 112-117.
4.    Bhat, N.V. and D.S. Wavhal, *Preparation of cellulose triacetate pervaporation membrane by ammonia plasma treatment.* Journal of Applied Polymer Science, 2000. **76**(2).
5.    Ku, J.R. and P. Stroeve, *Protein Diffusion in Charged Nanotubes:"On Off" Behavior of Molecular Transport.* Langmuir, 2004. **20**(5): p. 2030-2032.
6.    Merkina, E.E. and K.R. Fox, *Kinetic stability of intermolecular DNA quadruplexes.* Biophysical journal, 2005. **89**(1): p. 365-373.
7.    Liu, Y.S., et al., *Electrical characterization of DNA molecules in solution using impedance measurements.* Applied Physics Letters, 2008. **92**: p. 143902.
8.    Zhang, J., et al., *A gold nanoparticle-based chronocoulometric DNA sensor for amplified detection of DNA.* Nature Protocols, 2007. **2**(11): p. 2888.
9.    Mikkelsen, S.R., *Electrochemical Biosensors for DNA Sequence Detection.* ELECTROANALYSIS, 1996. **8**: p. 15-19.
10.   Itamar Willner and M. Zayats, *Electronic Aptamer-Based Sensors.* Angewandte Chemie International Edition, 2007. **46**(34): p. 6408-6418.
11.   Wei, F., et al., *Achieving differentiation of single-base mutations through hairpin oligonucleotide and electric potential control.* Biosensors and Bioelectronics, 2003. **18**(9): p. 1149-1155.
12.   Jin, Y., et al., *Hairpin DNA probe based electrochemical biosensor using methylene blue as hybridization indicator.* Biosensors & bioelectronics, 2007. **22**(6): p. 1126-1130.
13.   Kwakye, S. and A. Baeumner, *A microfluidic biosensor based on nucleic acid sequence recognition.* Analytical and bioanalytical chemistry, 2003. **376**(7): p. 1062-1068.
14.   Weigl, B.H. and P. Yager, *Microfluidics: microfluidic diffusion-based separation and detection.* Science, 1999. **283**(5400): p. 346.
15.   Choban, E.R., et al., *Microfluidic fuel cell based on laminar flow.* Journal of Power Sources, 2004. **128**(1): p. 54-60.
16.   Marie-Claire Bélanger, Y.M., *Hemocompatibility, biocompatibility, inflammatory and in vivo studies of primary reference materials low-density polyethylene and polydimethylsiloxane: A review.* Journal of Biomedical Materials Research, 2001. **58**(5): p. 467-477.
17.   Lotters, J.C., et al., *The mechanical properties of the rubber elastic polymer polydimethylsiloxane for sensor applications.* Journal of Micromechanics and Microengineering, 1997. **7**(3): p. 145-147.
18.   Brown, X.Q., K. Ookawa, and J.Y. Wong, *Evaluation of polydimethylsiloxane scaffolds with physiologically-relevant elastic moduli: interplay of substrate mechanics and surface chemistry effects on vascular smooth muscle cell response.* Biomaterials, 2005. **26**(16): p. 3123-3129.

19. Hasano Iu, A., et al., *Pervaporation separation of ethyl acetate–ethanol binary mixtures using polydimethylsiloxane membranes.* Chemical Engineering & Processing, 2005. **44**(3): p. 375-381.

20. Mohammadi, T., A. Aroujalian, and A. Bakhshi, *Pervaporation of dilute alcoholic mixtures using PDMS membrane.* Chemical engineering science, 2005. **60**(7): p. 1875-1880.

21. Balaban, N.Q., et al., *Force and focal adhesion assembly: a close relationship studied using elastic micropatterned substrates.* Nature cell biology, 2001. **3**(5): p. 466-472.

22. Madou, M.J., *Fundamentals of microfabrication: the science of miniaturization.* 2002: CRC.

23. MacDonald, S.M., et al., *Two-phase flow electrosynthesis: Comparing N-octyl-2-pyrrolidone-aqueous and acetonitrile-aqueous three-phase boundary reactions.* Journal of Physical Organic Chemistry, 2009. **22**(1).

24. Wu, H., et al., *Fabrication of complex three-dimensional microchannel systems in PDMS.* Burns. **190**: p. 197.

25. Liu, A., et al., *Rapid method for design and fabrication of passive micromixers in microfluidic devices using a direct-printing process.* Lab on a Chip, 2005. **5**(9): p. 974-978.

26. Wolfe, D.B., et al., *Customization of poly (dimethylsiloxane) stamps by micromachining using a femtosecond-pulsed laser.* Advanced Materials, 2003. **15**(1).

27. Mali, P., A. Sarkar, and R. Lal, *Facile fabrication of microfluidic systems using electron beam lithography.* Lab on a Chip, 2006. **6**(2): p. 310-315.

28. McDonald, J.C., et al., *Prototyping of microfluidic devices in poly (dimethylsiloxane) using solid-object printing.* Anal. Chem, 2002. **74**(7): p. 1537-1545.

29. Campbell, C.J., et al., *One-Step Multilevel Microfabrication by Reaction Diffusion.* Langmuir, 2005. **21**(1): p. 418-423.

30. Tolfree, D.W.L., *Microfabrication using synchrotron radiation.* Reports on Progress in Physics, 1998. **61**(4): p. 313-352.

31. Stroock, A.D. and M. Cabodi, *Microfluidic biomaterials.* MRS bulletin, 2006. **31**(2): p. 114-119.

32. Verma, M.K.S., A. Majumder, and A. Ghatak, *Embedded template-assisted fabrication of complex microchannels in PDMS and design of a microfluidic adhesive.* Langmuir, 2006. **22**(24): p. 10291-10295.

33. Asthana, A., et al., *Facile single step fabrication of microchannels with varying size.* Lab on a Chip, 2009. **9**(8): p. 1138-1142.

34. Juchniewicz, M., et al., *Porous crosslinked PDMS-microchannels coatings.* Sensors & Actuators: B. Chemical, 2007. **126**(1): p. 68-72.

35. Koktysh, D.S., et al., *Biomaterials by design: layer-by-layer assembled ion-selective and biocompatible films of TiO2 nanoshells for neurochemical monitoring.* Advanced Functional Materials, 2002. **12**(4).

36. Dinguizli, M., et al., *Development and evaluation of biocompatible films of polytetrafluoroethylene polymers holding lithium phthalocyanine crystals for their use in EPR oximetry.* Biosensors and Bioelectronics, 2006. **21**(7): p. 1015-1022.

37. Buchko, C.J., et al., *Processing and microstructural characterization of porous biocompatible protein polymer thin films.* POLYMER-LONDON-, 1999. **40**: p. 7397-7407.

38. Cui, F.Z. and D.J. Li, *A review of investigations on biocompatibility of diamond-like carbon and carbon nitride films.* Surface & Coatings Technology, 2000. **131**(1-3): p. 481-487.

39. Cotell, C.M., *Pulsed laser deposition and processing of biocompatible hydroxylapatite thin films.* Appl Surf Sci, 1993. **69**: p. 140–148.

57

40.     Albornoz, C. and S.E. Jacobo, *Preparation of a biocompatible magnetic film from an aqueous ferrofluid.* Journal of Magnetism and Magnetic Materials, 2006. **305**(1): p. 12-15.
41.     Chu, P.K., et al., *Plasma-surface modification of biomaterials.* Materials Science & Engineering R, 2002. **36**(5-6): p. 143-206.
42.     Muguruma, H. and I. Karube, *Plasma-polymerized films for biosensors.* Trends in Analytical Chemistry, 1999. **18**(1): p. 62-68.
43.     Cunningham, A.J. and R.H. Austin, *Introduction to bioanalytical sensors.* Physics Today, 1999. **52**(6).
44.     Lewis, J.S. and M.S. Weaver, *Thin-film permeation-barrier technology for flexible organic light-emitting devices.* IEEE Journal of selected topics in quantum electronics, 2004. **10**(1): p. 45-57.
45.     Flink, S., F. Van Veggel, and D.N. Reinhoudt, *Sensor functionalities in self-assembled monolayers.* Advanced Materials, 2000. **12**(18).
46.     Jin, Y., et al., *Controlled nucleation and growth of surface-confined gold nanoparticles on a (3-aminopropyl) trimethoxysilane-modified glass slide: a strategy for SPR substrates.* Anal. Chem, 2001. **73**(13): p. 2843-2849.
47.     Espinola, J.G.P., et al., *Chemisorption of CuII and CoII chlorides and -diketonates on silica gel functionalized with 3-aminopropyltrimethoxysilane.* Colloids and Surfaces A: Physicochemical and Engineering Aspects, 2000. **166**(1-3): p. 45-50.
48.     Nakanishi, K., H. Muguruma, and I. Karube, *A novel method of immobilizing antibodies on a quartz crystal microbalance using plasma-polymerized films for immunosensors.* Anal. chem, 1996. **68**(10): p. 1695-1700.
49.     Manning, M., et al., *A versatile multi-platform biochip surface attachment chemistry.* Materials Science & Engineering C, 2003. **23**(3): p. 347-351.
50.     Maddox, P.H. and D. Jenkins, *3-Aminopropyltriethoxysilane (APES): a new advance in section adhesion.* British Medical Journal, 1987. **40**(10): p. 1256-1257.
51.     Low, S.P., et al., *Evaluation of mammalian cell adhesion on surface-modified porous silicon.* Biomaterials, 2006. **27**(26): p. 4538-4546.
52.     Bennès, J., S. Ballandras, and F. Chérioux, *Easy and versatile functionalization of lithium niobate wafers by hydrophobic trichlorosilanes.* Applied Surface Science, 2008. **255**(5P1): p. 1796-1800.
53.     Lee, K.K., B. Bhushan, and D. Hansford, *Nanotribological characterization of fluoropolymer thin films for biomedical micro/nanoelectromechanical system applications.* Journal of Vacuum Science & Technology A: Vacuum, Surfaces, and Films, 2005. **23**: p. 804.
54.     Hozumi, A., et al., *Amino-terminated self-assembled monolayer on a SiO surface formed by chemical vapor deposition.* Journal of Vacuum Science & Technology A: Vacuum, Surfaces, and Films, 2001. **19**: p. 1812.
55.     Allen, G.C., et al., *Macro-, micro-and nano-investigations on 3-aminopropyltrimethoxysilane self-assembly-monolayers.* Thin Solid Films, 2005. **483**(1-2): p. 306-311.
56.     Colorado Jr, R. and T.R. Lee, *Wettabilies of self-assembled monolayers on gold generated from progressively fluorinated alkanethiols.* J. Phys. Chem. B, 2000. **104**: p. 7417.
57.     Yamabe, M. and M. Matsuo, *Newest Aspect of Fluoro Functional Material*. 1994, CMC Press, Tokyo.
58.     Scheirs, J., *Modern fluoropolymers*. 1997: Wiley New York.
59.     Ho, J.Y., T. Matsuura, and J.P. Santerre, *The effect of fluorinated surface modifying macromolecules on the surface morphology of polyethersulfone membranes.* Journal of biomaterials science. Polymer edition, 2000. **11**(10): p. 1085.

60.     Clarotti, G., et al., *Modification of the biocompatible and haemocompatible properties of polymer substrates by plasma-deposited fluorocarbon coatings.* Biomaterials, 1992. **13**(12): p. 832-840.

61.     Kaku, M., et al., *New fluorinated oxazoline block copolymer lowers the adhesion of platelets on polyurethane surfaces.* Journal of Polymer Science Part A: Polymer Chemistry, 1994. **32**(11).

62.     Zhang, Y., et al., *Characterization of fluoropolymer films deposited by magnetron sputtering of poly (tetrafluoroethylene) and plasma polymerization of heptadecafluoro-1-decene (HDFD) on (100)-oriented single-crystal silicon substrates.* Surface and Interface Analysis, 2002. **34**(1): p. 10-18.

63.     Durrant, S.F., R.P. Mota, and M.A.B. de Moraes, *Fluorinated polymer films from r. f. plasmas containing benzene and sulfur hexafluorine.* Thin Solid Films, 1992. **220**(1): p. 295-302.

64.     Li, S.T., et al., *Pulsed-laser deposition of crystalline Teflon (PTFE) films.* Applied Surface Science, 1998. **125**(1): p. 17-22.

65.     Lau, K.K.S. and K.K. Gleason, *Thermal annealing of fluorocarbon films grown by hot filament chemical vapor deposition.* J. Phys. Chem. B, 2001. **105**(12): p. 2303-2307.

66.     Sharangpani, R., et al., *Chemical vapor deposition and characterization of amorphous teflon fluoropolymerthin films.* Journal of Electronic Materials, 1997. **26**(4): p. 402-409.

67.     Zhou, Y., et al., *Synthesis of hyperbranched, hydrophilic fluorinated surface grafts.* Langmuir, 1996. **12**(23): p. 5519-5521.

68.     Prucker, O. and J. Ruhe, *Synthesis of poly (styrene) monolayers attached to high surface area silica gels through self-assembled monolayers of azo initiators.* Macromolecules, 1998. **31**(3): p. 592-601.

69.     Jeyaprakash, J.D., S. Samuel, and J. Ruhe, *A facile photochemical surface modification technique for the generation of microstructured fluorinated surfaces.* Langmuir, 2004. **20**(23): p. 10080-10085.

70.     Wang, X.L. and S. Suda, *Stability and tolerance to impurities of the fluorinated surface of hydrogen-absorbing alloys.* Journal of Alloys and Compounds, 1995. **227**(1): p. 58-62.

71.     Liu, F.J. and S. Suda, *A method for improving the long-term storability of hydriding alloys by air/water exposure.* Journal of alloys and compounds, 1995. **231**(1-2): p. 411-416.

72.     Iqbal, S.M., D. Akin, and R. Bashir, *Solid-state nanopore channels with DNA selectivity.* Nature Nanotechnology, 2007. **2**(4): p. 243-248.

73.     Lu, W., et al., *Label-free photoelectrochemical strategy for hairpin DNA hybridization detection on titanium dioxide electrode.* Applied Physics Letters, 2006. **89**: p. 263902.

74.     Kohli, P., et al., *DNA-functionalized nanotube membranes with single-base mismatch selectivity.* Science, 2004. **305**(5686): p. 984.

75.     Storhoff, J.J., et al., *One-pot colorimetric differentiation of polynucleotides with single base imperfections using gold nanoparticle probes.* Journal of the American Chemical Society, 1998. **120**(9): p. 1959-1964.

76.     http://rsb.info.nih.gov/ij/.

77.     Wang, W., T. Lee, and M.A. Reed, *Mechanism of electron conduction in self-assembled alkanethiol monolayer devices.* Physical Review B, 2003. **68**(3): p. 35416.

78.     Kindt, T.J., B.A. Osborne, and R.A. Goldsby, *Antigen-Antibody interactions: Principles and applications*, in *Kuby Immunology*. 2006, W.H. Freeman Biology. p. 145-146.

79.     Bauer, W.R. and W. Nadler, *Molecular transport through channels and pores: Effects of in-channel interactions and blocking.* Proceedings of the National Academy of Sciences, 2006. **103**: p. 11446-11451.

80.     Mulder, M., *Basic Principles of Membrane Technology*. 1996: Springer.

81. Panchuk–Voloshina, N., et al., *Alexa Dyes, a Series of New Fluorescent Dyes that Yield Exceptionally Bright, Photostable Conjugates.* Journal of Histochemistry and Cytochemistry, 1999. **47**(9): p. 1179.

82. Ferain, E. and R. Legras, *Track-etched membrane: dynamics of pore formation.* Nuclear Instruments and Methods in Physics Research B, 1994. **84**: p. 331-336.

83. Hillborg, H. and U.W. Gedde, *Hydrophobicity recovery of polydimethylsiloxane after exposure to corona discharges.* Polymer, 1998. **39**(10): p. 1991-1998.

84. Chambon, F. and H.H. Winter, *Linear viscoelasticity at the gel point of a crosslinking PDMS with imbalanced stoichiometry.* Journal of Rheology, 1987. **31**(8): p. 683-697.

85. Paul, J.F. and John Rehner, Jr., *Statistical Mechanics of Cross-Linked Polymer Networks I. Rubberlike Elasticity.* The Journal of Chemical Physics, 1943. **11**(11): p. 512-520.

86. Flory, P.J. and W.R. Krigbaum, *Thermodynamics of high polymer solutions.* Annual review of physical chemistry, 1951. **2**(1): p. 383-402.

87. Giannelis, E.P., *Polymer Layered Silicate Nanocomposites.* Advanced Materials, 1996. **8**(1): p. 29–35.

88. Keleser, S., et al., *Desorption of ethylacetate–water mixture by using crosslinked polydimethylsiloxane membrane.* Desalination, 2006. **200**(1-3): p. 44-45.

89. Lee, J.N., C. Park, and G.M. Whitesides, *Solvent Compatibility of Poly (dimethylsiloxane)-Based Microfluidic Devices.* ANALYTICAL CHEMISTRY-WASHINGTON DC-, 2003. **75**(23): p. 6544-6554.

90. Apel, P., *Track etching technique in membrane technology.* Radiation measurements, 2001. **34**(1-6): p. 559-566.

91. Puntes, V.F., K.M. Krishnan, and A.P. Alivisatos, *Colloidal Nanocrystal Shape and Size Control: The Case of Cobalt.* 2001. p. 2115-2117.

92. Chien, C.L., et al., *Electrodeposited magnetic nanowires: arrays, field-induced assembly, and surface functionalization.* Journal of Magnetism and Magnetic Materials, 2002. **249**(1-2): p. 146-155.

93. Chang, H., et al., *DNA counterion current and saturation examined by a MEMS-based solid state nanopore sensor.* Biomedical Microdevices, 2006. **8**(3): p. 263-269.

94. Smeets, R.M.M., et al., *Salt dependence of ion transport and DNA translocation through solid-state nanopores.* Nano Lett., 2006. **6**(1): p. 89-95.

95. Jackman, R.J., et al., *Using elastomeric membranes as dry resists and for dry lift-off.* Langmuir, 1999. **15**(8): p. 2973-2984.

96. Ray, V., et al., *CMOS-compatible fabrication of room-temperature single-electron devices.* Nat Nano, 2008. **3**(10): p. 603-608.

97. Huang, H.W., et al., *Single-particle placement via self-limiting electrostatic gating.* Applied Physics Letters, 2008. **93**: p. 073110.

98. Ma, L.C., et al., *Electrostatic Funneling for Precise Nanoparticle Placement: A Route to Wafer-Scale Integration.* Nano Lett, 2007. **7**(2): p. 439-445.

99. Kuo, Y.C. and T.W. Lin, *Electrophoretic Mobility, Zeta Potential, and Fixed Charge Density of Bovine Knee Chondrocytes, Methyl Methacrylate Sulfopropyl Methacrylate, Polybutylcyanoacrylate, and Solid Lipid Nanoparticles.* J. Phys. Chem. B, 2006. **110**(5): p. 2202-2208.

BIOGRAPHICAL INFORMATION

Swati Goyal was born on November 10, 1984 in Karnal, India where she grew up and completed her high school.  She moved to Ambala to complete her undergraduate studies in Biotechnology Engineering at Ambala College of Engineering, Kurukshetra University where she also worked as research assistant with Dr. Amit Asthana post undergraduation. She worked as Lecturer of Immunology and Biochemistry at Rajasthan University before she moved to University of Texas at Arlington in 2009 for masters in science in Biomedical Engineering.  She has been working towards here masters under supervision of Dr. Samir M. Iqbal since January 2008.